

ARTICLE

IQSEC2/BRAG1 may modulate postsynaptic density assembly through Ca²⁺-induced phase separation

Guanhua Bai¹*, Ruifeng Huang¹*, Xinyue Nan^{2,3}*, Mengru Zhuang¹, Meiling Wu¹, Yinmiao Lian^{2,3}, Qixu Cai⁴, Honglei Tian⁵, Youming Lu^{2,3}, Hao Li^{2,3}, and Mingjie Zhang¹

IQSEC2, a high-confidence neurodevelopmental disorder risk gene product, is essential for neuronal development and synaptic plasticity. Previous studies established that IQSEC2 dynamically regulates synaptic signaling via Ca²⁺-dependent release of autoinhibition. In this study, using *in vivo* mouse models and *in vitro* biochemistry approaches, we discover that IQSEC2 orchestrates postsynaptic density assembly and dynamics via Ca²⁺-triggered phase separation. Mechanistically, Ca²⁺-induced conformational opening leads to phase separation-mediated condensation of IQSEC2 at synapses, a process that requires the N-terminal multimerization domain and intrinsically disordered regions of IQSEC2. We identified a single-point mutation, F367A, in IQSEC2, which exhibits constitutive activity by structurally mimicking the Ca²⁺-activated state of the WT protein. Mice carrying the *Iqsec2_F367A* mutation have elevated basal synaptic transmission and impaired activity-dependent plasticity assayed in hippocampal neurons and spatial learning deficits. Thus, IQSEC2 can bidirectionally modulate synaptic strengths via Ca²⁺-dependent phase separation, and dysregulation of phase separation may be a contributing factor in IQSEC2-related neurodevelopmental disorders.

Introduction

The IQSEC (IQ motif and Sec7 domain-containing protein, also known as BRAG for brefeldin A-resistant guanine nucleotide exchange factor [GEF]) family proteins are a class of ARF-GEFs, each containing a Sec7 domain with GEF activity. Among the three family members, IQSEC2 is specifically expressed in the central nervous system, where it plays pivotal roles in neuronal development and synaptic plasticity. Mutations of the *IQSEC2* have been found in many patients with intellectual disability (ID), often accompanied by other physical, neurological, or psychiatric symptoms (Shoubridge et al., 2019).

IQSEC2 was originally identified as a major component in the excitatory postsynaptic density (PSD) by mass spectrometry (Murphy et al., 2006). The protein is highly expressed in the adult rat forebrain, strongly enriched in the "core" PSD fraction, and forms discrete clusters with PSD-95 at excitatory synapses (Sakagami et al., 2008). Quantitative mass spectrometry measurements revealed the relative molar ratio of IQSEC2 to PSD-95 is 0.11 \pm 0.05, and IQSEC2 is at a comparable abundance with that of N-methyl-D-aspartate (NMDA) receptors (NMDARs) or α -amino-3-hydroxy-5-methyl-4-isoxazole propionic acid (AMPA) receptors (AMPARs) (Dosemeci et al., 2007; Lowenthal et al., 2015). The high

abundance of IQSEC2 in synapses suggests a possible prominent role of the enzyme in synaptic functions.

Most studies have focused on IQSEC2's ARF-GEF activity and its dysregulation in neurodevelopmental disorders. In hippocampal neurons, IQSEC2 activates ARF6 to trigger the AMPAR internalization upon long-term depression (LTD) induction (Brown et al., 2016; Myers et al., 2012; Rogers et al., 2019). Since the regulation of AMPAR trafficking is closely related to synaptic plasticity, which underlies the molecular basis of learning and memory, the dysregulation of the IQSEC2 GEF activity may account for neurological deficits such as cognitive impairments for many of the IQSEC2 mutations found in patients.

However, independent of its GEF activity and synaptic activity, the incorporation of IQSEC2 into the PSD through interactions with scaffolds or membrane proteins, such as PSD scaffold protein PSD-95 (Sakagami et al., 2008) or IRsp53 (Sanda et al., 2009), has also been reported to enhance the synaptic transmission in a dose-dependent way (Brown et al., 2016). These studies suggest that, in addition to acting as a GEF, IQSEC2 may also play structural roles in modulating synaptic functions. Either reduction or overexpression of IQSEC2 in mouse hippocampal neurons led to significant neuronal morphology changes

¹School of Life Sciences, Southern University of Science and Technology, Shenzhen, China; ²Department of Pathophysiology, School of Basic Medicine and Tongji Medical College, Huazhong University of Science and Technology, Wuhan, China; ³Innovation Center for Brain Medical Sciences of the Ministry of Education, Huazhong University of Science and Technology, Wuhan, China; ⁴State Key Laboratory of Vaccines for Infectious Diseases, School of Public Health, Xiamen University, Xiamen, China; ⁵HKUST Jockey Club Institute for Advanced Study and Division of Life Science, The Hong Kong University of Science and Technology, Hong Kong, China.

*G. Bai, R. Huang, and X. Nan contributed equally to this paper. Correspondence to Mingjie Zhang: zhangmj@sustech.edu.cn; Hao Li: lihaochn@hust.edu.cn.

© 2025 Bai et al. This article is distributed under the terms as described at https://rupress.org/pages/terms102024/.





as well as dendritic spine alternations (Hinze et al., 2017). In addition, patients carrying frameshift mutations (p.G1468Afs*27, p.S1474Rfs*17, p.S1474Vfs*21, and p.S1474Qfs*133) in the very C-terminal of IQSEC2, which encompassed the PDZ-binding motif (PBM) required for its localization in the PSD, have moderate to severe ID, autism, and speech deficits, suggesting that the functionality of IQSEC2 in the PSD relies on its specific spatial localization (Lopergolo et al., 2021; Radley et al., 2019; Shoubridge et al., 2019).

IQSEC2 possesses multiple structural and functional domains that potentially endow the enzyme to play distinct roles in response to different input signals (Petersen et al., 2020). We recently demonstrated that IQSEC2 adopts an autoinhibited conformation that can be released by Ca²⁺ (Bai et al., 2023). IQSEC2 is inactive under the resting condition as the ARFbinding site on the Sec7-PH tandem of IQSEC2 is blocked by its IQ motif in complex with apo-CaM. Ca²⁺ binding to CaM triggers dissociation of Ca2+-CaM-bound IQ motif from the Sec7-PH tandem and concomitant activation of the enzyme. Consistent with this model, mice with a single missense mutation either perturbing Ca2+-induced GEF activity regulation (R359C or A350V, both with higher basal GEF activities) or directly causing GEF activity impairment (Q801P, with near null GEF activity even under the Ca²⁺-saturated condition) had impaired LTD accompanied by LTD-dependent retrieval memory deficits. Curiously, we observed abnormally quick ceiling effects in longterm potentiation (LTP) and autistic behaviors in R359C mice, but not in Q801P mice. Although the Q801P mutation of IQSEC2 loses its GEF activity, the mutant protein still displays Ca2+-induced conformation opening like the WT protein does (Bai et al., 2023). It is further noted that IQSEC2 knockout mice (Mehta et al., 2021; Sah et al., 2020), as well as mice containing the R359C or A350V mutations, exhibit stronger phenotypic deficits than mice containing the Q801P mutation (Bai et al., 2023). These results collectively indicate that the Ca2+-regulated structural role of IQSEC2, in addition to its GEF activity, is also essential for IQSEC2 to function properly in the nervous system. However, it is not known how IQSEC2 may play structural roles in synaptic functions.

In this study, we generated a knock-in mouse model carrying an IQSEC2 single-point mutation with Phe367 substituted with Ala (F367A). The F367A mutation is constitutively active, as its IQ motif is dissociated from the Sec7-PH tandem, and thus the mutant mimics the Ca2+-bound form of the enzyme. Mice carrying the F367A mutation displayed a ceiling effect in LTP and cognitive deficits as observed in mice carrying R359C or A350V mutations (Bai et al., 2023). The F367A mice also exhibited enhanced basal synaptic strength through postsynaptic mechanisms, including enlarged dendritic spines, elevated levels of PSD-95 and AMPARs at the PSD, and enlarged PSD areas. We discovered that IQSEC2 undergoes Ca2+-dependent phase separation. This Ca²⁺-regulated phase separation likely underpins IQSEC2's ability to dynamically modulate postsynaptic protein complexes. The constitutively open form of IQSEC2_F367A loses IQSEC2-mediated, Ca²⁺-dependent PSD condensate dynamic regulation, which may underlie the synaptic and behavioral abnormalities observed in the mutant mice.

Results

The F367A mutant is conformationally open and mimics the Ca²⁺-bound state of fully active IQSEC2

We previously elucidated the structural basis underlying the Ca²⁺-dependent conformational change of IQSEC2 (Fig. 1 A) (Bai et al., 2023). In that study, we examined the pathogenic R359C, A350V, and A350D mutations identified in patients. All these missense mutations impair the interaction between the IQ motif and apo-CaM, causing weakened intramolecular coupling between the unbound IQ motif and the Sec7-PH tandem (Fig. 1, A and B). Additionally, the exposure of the isolated IQ motif in the R359C and A350V/D mutants of IQ-SEC2 causes the mutant proteins to be less stable and prone to aggregation, creating a technical issue for mechanistic studies of these mutants.

To generate a better model for investigating the Ca2+-dependent function of IQSEC2 while mitigating the poor protein quality encountered in previous mutants, we designed another single-site mutation with Phe367 substituted by Ala (F367A). This mutation was strategically designed to disrupt intramolecular coupling without compromising protein stability. Phe367 is located at the C-terminal end of the α 2-helix but outside the consensus IQ motif (Fig. 1 C). We therefore predicted that the F367A substitution would preserve the binding of both apo- and Ca²⁺-CaM to the IQ motif of IQSEC2 (Fig. 1, D-G). Consistent with our prediction, the F367A mutant formed stable complexes with both apo-CaM and Ca2+-CaM in solution, as confirmed by sizeexclusion chromatography (SEC) (Fig. 1E, red curve). Isothermal titration calorimetry (ITC) measured the affinity of apo-CaM for the F367A mutant (K_D = 34.4 nM) to be ~30-fold weaker than the apparent affinity for the WT protein ($K_D = 1.13 \text{ nM}$). It should be noted that the WT value represents the combined binding of apo-CaM to the IQ motif and subsequent intramolecular docking to Sec7-PH (Bai et al., 2023). In contrast, the F367A value reports the direct CaM-IQ interaction, as the mutation disrupts the coupling between IQ_F367A/apo-CaM and Sec7-PH (Fig. 1, E-G, left panel). The K_D of apo-CaM/IQ binding to the Sec7-PH tandem (i.e., the apo-CaM/IQ and Sec7-PH coupling strength) is \sim 2 μ M (Bai et al., 2023). We thus interpreted that the apo-CaM/IQ binding was not affected by the F367A mutation. It is further noted that synaptic CaM concentrations (\sim 10 μ M) vastly exceed the measured K_D values for CaM binding to WT or F367A IQSEC2, meaning that their IQ motif is fully saturated by CaM under physiological conditions, regardless of synaptic Ca²⁺ levels.

As expected, the Ca²⁺-CaM-bound IQ motif of the F367A mutant remains dissociated from the Sec7-PH tandem (Fig. 1, E-G, right panels). Thus, the F367A mutant of IQSEC2 adopts a constitutively open conformation with its catalytic Sec7-PH tandem permanently accessible for ARF binding and activation regardless of cellular Ca²⁺ signals. Consequently, the F367A mutant exhibits high basal GEF activity equivalent to the Ca²⁺ activated WT enzyme (Fig. 1 D). In sum, the F367A mutant faithfully mimics the Ca²⁺-bound, active-state conformation of IQSEC2 but is uncoupled from the Ca²⁺ regulation, providing a unique tool to dissect the functional consequences of constitutive activation.



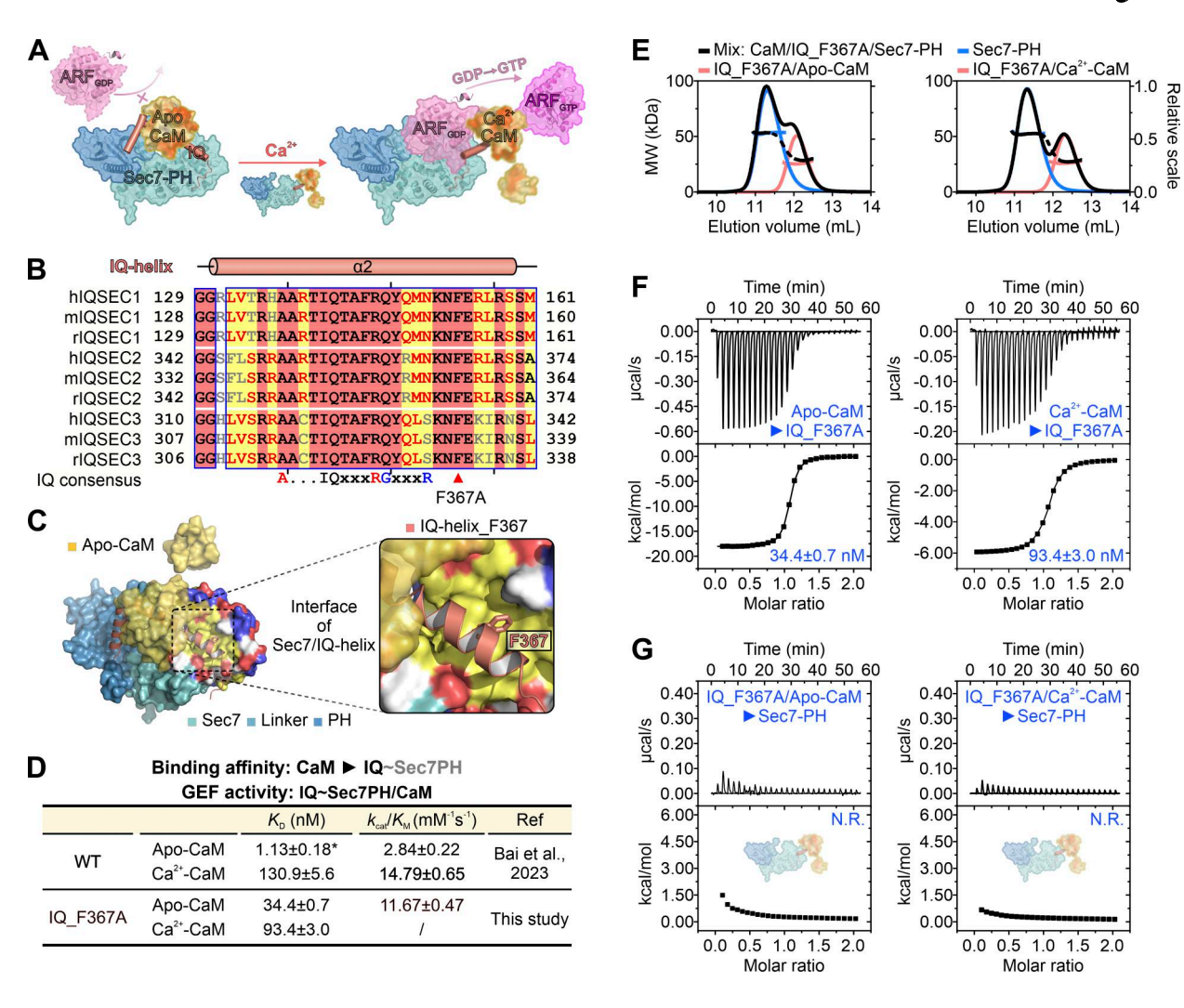


Figure 1. The F367A mutant is conformationally open, constitutively active, and mimics the Ca²⁺-bound state of IQSEC2. (A) Schematic model of IQSEC2 autoinhibition in the apo-CaM-bound form and the Ca²⁺-dependent conformational opening and activation of its ARF GEF activity. (B) Sequence alignment analysis of the IQ motif from IQSECs. Phe367 is denoted by a red triangle. (C) The detailed interactions surrounding Phe367 in IQSECs are illustrated by the structure of the apo-CaM/IQ/Sec7-PH ternary complex (PDB accession no. 7VMB). (D) Summary of the effects of the F367A mutation on CaM-IQ binding and GEF activity in the absence and presence of Ca²⁺. (E) Size-exclusion chromatography coupled with multiangle light scattering (SEC-MALS) analysis indicates that the IQ_F367A/CaM complex failed to associate with the Sec7-PH tandem, as evidenced by the absence of peak shifts or increased molecular mass in the elution profiles under both Ca²⁺-free and Ca²⁺-saturated conditions. (F) ITC thermograms and titration plots of 100 μM CaM into 10 μM IQ~Sec7PH_F367A protein in the absence and presence of Ca²⁺. (G) ITC thermograms and titration plots of 200 μM IQ_F367A/CaM complex into 20 μM Sec7-PH protein in the absence and presence of Ca²⁺. N.R., fitting is not reliable due to the very weak binding. PDB, Protein Data Bank.

IQSEC2 F367A mice display altered synaptic transmission, reduced LTP, and cognitive impairments

To determine whether the altered LTP and autistic behaviors observed in mutant mice with missense mutations in the IQ motif are specifically attributed to the loss of the Ca²⁺ switch caused by the mutations, we generated a knock-in mouse carrying the F367A mutation (Fig. 2, A and B). In contrast to the R359C mutant (Bai et al., 2023), IQSEC2 F367A mice displayed no abnormalities in 24-h spontaneous behavior recordings, which assessed their natural behavioral patterns in a home cage environment (Fig. S1, A–D). In the open-field test, F367A mice exhibited comparable total distance traveled and time spent in the center zone with WT controls (Fig. S1, E and F). Similarly, elevated plus maze tests showed no genotype-dependent differences in moving distance or time spent in open arms (Fig. S1, G

and H), confirming intact locomotor activity as well as normal physical and mental conditions.

Surprisingly, synaptic transmissions were significantly elevated in IQSEC2 F367A mutant neurons compared with neurons from the WT littermates. We assessed miniature and spontaneous excitatory postsynaptic currents (mEPSCs and sEPSCs) in CA1 pyramidal neurons from acute hippocampal slices. While the mean frequency of mEPSCs was unchanged between IQSEC2 F367A mutants and controls, the cumulative distribution of synaptic event amplitudes exhibited a rightward shift, reflecting a significant increase in mEPSC amplitude in mutants (Fig. 2 C). This indicates enhanced quantal size of AMPAR-mediated currents at postsynaptic sites. Direct measurements of action potential-evoked excitatory postsynaptic currents (eEPSCs) revealed a significant increase in AMPAR-mediated responses in



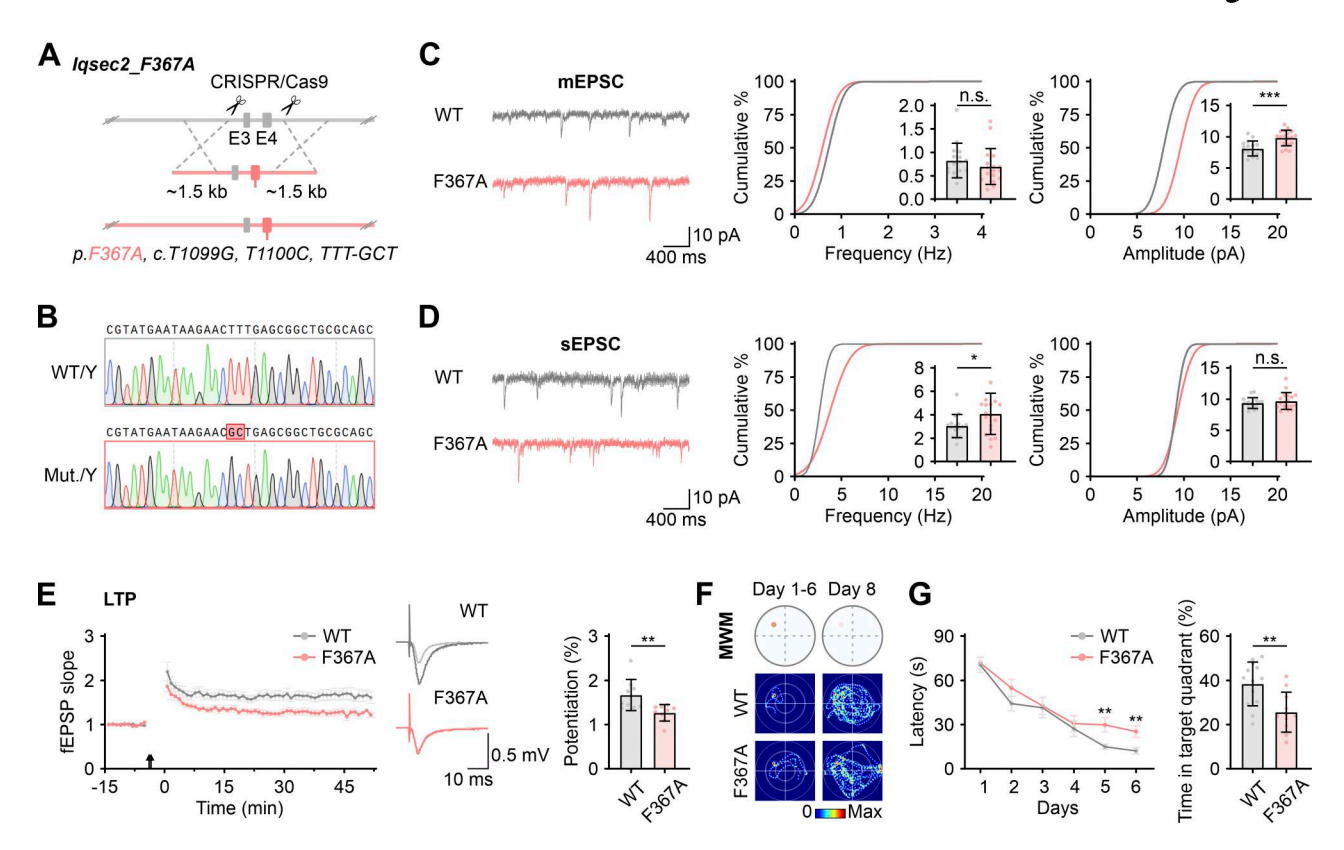


Figure 2. IQSEC2 F367A mice display altered synaptic transmission, reduced LTP, and cognitive impairments. (A) Schematic strategy for generating IQSEC2 F367A mice using CRISPR/Cas9. sgRNA recognition sites are indicated with scissors. (B) Representative DNA sequencing results from WT and hemizygous mice highlighted substituted sequences. (C and D) Representative traces and comparison of mEPSC (C) or sEPSC (D) frequency and amplitude cumulative probability distributions recorded from CA1 pyramidal neurons from F367A mutant mice and their WT littermates. Insets show average values per neuron for frequency and amplitude. Data are presented as mean ± SD (16 neurons from 3 mice per group; n.s., not significant; *P < 0.05; ***P < 0.001; unpaired t test). (E) Plots showing the time course (left) and the summarized values 20 min post-tetanus (right) for the normalized fEPSP slope in hippocampal slices from F367A mutant mice and their WT littermates. The fEPSP slope (5–95%) was normalized to the baseline period (defined as 1.0) immediately preceding the first tetanus (↑). Data are presented as mean ± SD (9 slices from 3 mice per group; **P < 0.01; unpaired t test). Sample traces show the baseline and sweep at 45 min following tetanus. (F) Scheme of the Morris water maze (MWM) experiment and representative exploration trajectories on the sixth day during training and the eighth (probe test) day in the MWM. (G) Left: The escape latency during training in the MWM to reach the hidden platform. Data are presented as mean ± SEM. Right: Quantification of time spent in the target quadrant in the probe trial on the eighth day. Data are presented as mean ± SD (WT: 13 mice; F367A: 11 mice; **P < 0.01; unpaired t test).

F367A neurons, with no significant changes in NMDAR-mediated responses, leading to a trend toward an elevated AMPAR: NMDAR current ratio (Fig. S1, I-K). In contrast, sEPSCs in F367A neurons showed a nonsignificant trend toward larger amplitudes compared with WT, alongside a modest elevation in sEPSC frequency (Fig. 2 D), potentially implicating presynaptic or network-level modifications. Collectively, these data indicate that the IQSEC2 F367A mutation enhances basal synaptic strength primarily through postsynaptic mechanisms, possibly by increased AMPAR abundance or synaptic scaling, with additional subtle contributions from altered network excitability.

To investigate whether heightened synaptic transmission in IQSEC2 F367A mutant mice compromises plasticity, we measured LTP at Schaffer collateral CA1 synapses. F367A mutants exhibited significantly reduced LTP magnitude compared with the WT controls (Fig. 2 E). One possible interpretation is that the elevated basal AMPAR transmission partially occludes LTP expression. This LTP occlusion may result from smaller dynamic

ranges of synaptic potentiation due to loss of Ca²⁺-dependent IQSEC2 activation (see below for more details).

Consistent with their reduced LTP, F367A mutant mice exhibited pronounced deficits in spatial learning and memory during Morris water maze testing. Compared with WT littermates, F367A mutants demonstrated significantly longer escape latencies during training sessions (Fig. 2, F and G), indicating impaired spatial navigation to a hidden platform by visual cues. On day 8, probe trials (with the platform removed) revealed that F367A mice spent substantially less time in the target quadrant (Fig. 2, F and G), revealing compromised memory retention of the mutant mice.

The enhanced basal synaptic transmissions of the IQSEC2 F367A mutation observed in our study are in apparent contradiction with the enhanced GEF activity of the mutant. Given that AMPAR internalization requires the GEF activity of IQSEC2 (Myers et al., 2012), one would predict that IQSEC2 F367A mice should have weakened basal synaptic transmissions. As we will show below, this apparent contradiction can be reconciled by



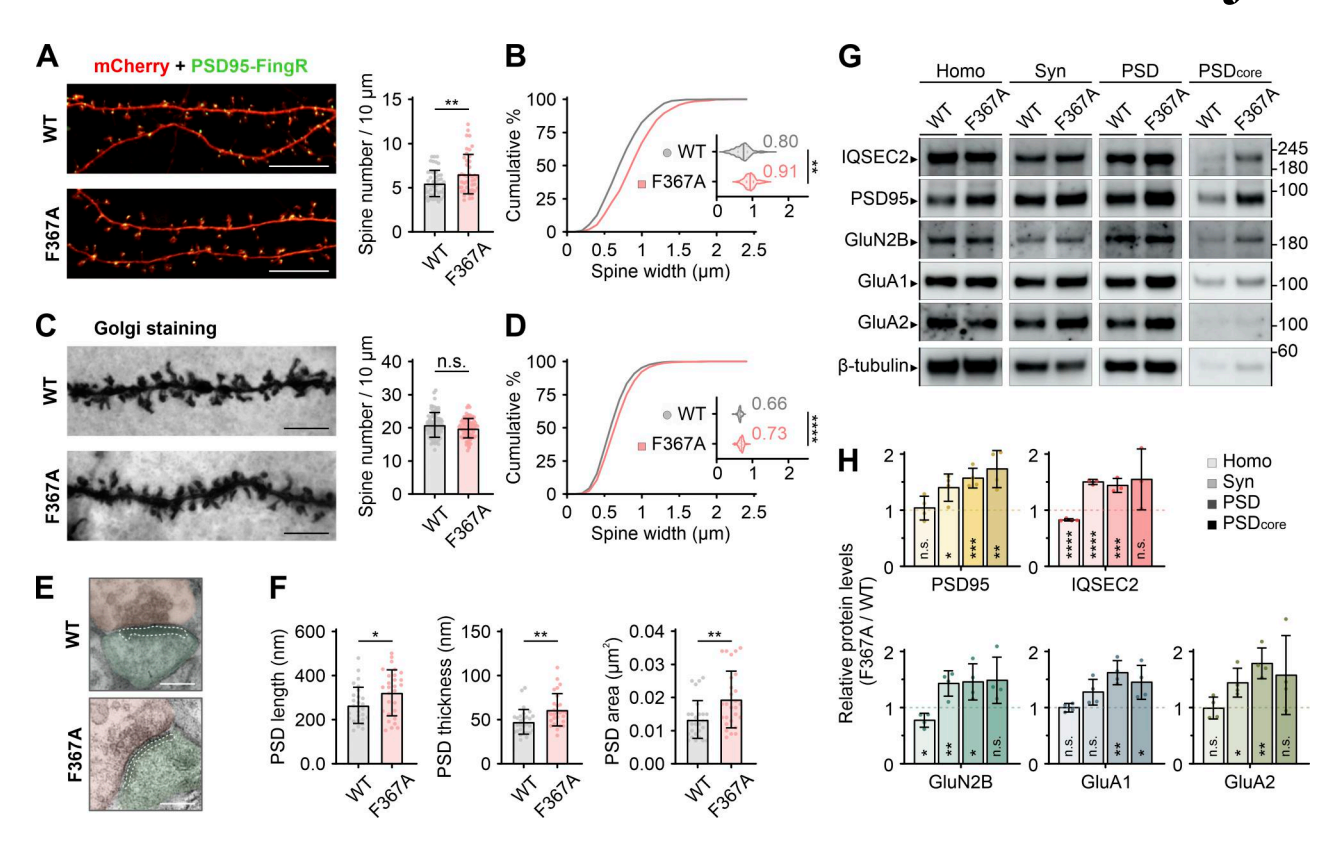


Figure 3. IQSEC2 F367A mutant promotes spine enlargement and postsynaptic protein enrichment. (A) Representative fluorescent images showing secondary dendrites of cultured hippocampal neurons from F367A mutant mice and their WT littermates. mCherry and PSD95-FingR were co-transfected as morphological and excitatory postsynaptic markers. Scale bar, 10 μm. Quantification of spine density indicates increased spine numbers in F367A mutant mice. Data are presented as mean ± SD (WT: 48 dendrites from 14 neurons, 8 cultures; F367A: 44 dendrites from 14 neurons, 5 cultures; **P < 0.01; unpaired t test). (B) Cumulative probability distribution of spine width measurements from dendrites of cultured hippocampal neurons. Insets show violin plots of mean spine width per neuron. Data are presented as median and quartiles (WT: 1,303 spines from 14 neurons, 8 cultures; F367A: 1,198 spines from 14 neurons, 5 cultures; **P < 0.01; nested t test within neurons). (C) Representative confocal images and quantification of spine number on secondary dendrites of Golgi-stained CA1 pyramidal neurons. Scale bar, 5 μm. Data are presented as mean ± SD (WT/F367A: 80 dendrites from 4 mice per group; n.s., not significant; unpaired t test). (D) Cumulative probability distribution of spine width measurements from dendrites of Golgi-stained pyramidal neurons. Insets show violin plots of mean spine width per dendrite. Data are presented as median and quartiles (WT: 6,262 spines; F367A: 5,656 spines; 80 dendrites from 4 mice per group; ****P < 0.0001; nested t test within dendrites). (E) Representative electron micrographs of CA1 synapses. Postsynaptic spines (green) and PSDs (dashed lines) are indicated. Scale bar, 200 nm. (F) Measurement of PSD length, thickness, and area from electron micrographs. Data are presented as mean ± SD (28 synapses from 4 mice per group; *P < 0.05; **P < 0.01; unpaired t test). (G) Representative western blots showing biochemical fractionation of hippocampus from F367A mutant mice and their respective WT littermates. The different fractions analyzed were as follows: Homo, homogenate of adult mouse hippocampus; Syn, synaptosome fraction (enriched with synaptic membranes); PSD, the pellet obtained after two rounds of extraction of synaptosomes with Triton X-100; PSD_{core}, the pellet obtained after sarcosyl extraction of the crude PSD pellet. The loading control of the PSD core fraction was the same as the PSD fraction, as the extraction started with two identical portions of synaptosome fractions. (H) Quantitative analyses of protein abundance in different subcellular fractions. Densitometric scans of immunoblots were obtained from three to four independent experiments. Data were presented as relative levels of each protein compared with their WT values, after normalizing for β-tubulin protein expression levels in each fraction. The PSD_{core} fraction was normalized with the β-tubulin protein levels in the crude PSD fraction, as the PSD_{core} was derived from this fraction with one round of sarcosyl extraction. (n.s., not significant; *P < 0.05; **P < 0.01; ***P < 0.001; ****P <0.0001; unpaired t test). Source data are available for this figure: SourceData F3.

 ${
m Ca^{2+}}$ -dependent structural roles of IQSEC2 in organizing the PSD assemblies.

IQSEC2 F367A mutant promotes spine enlargement and postsynaptic protein enrichment

To further elucidate the molecular mechanisms underlying the enhanced basal synaptic transmissions observed in F367A mice, we analyzed spine morphologies of hippocampal pyramidal neurons derived from WT and F367A mice. Cultured F367A neurons exhibited significantly increased dendritic spine density and larger spine sizes when compared with spines in WT neurons (Fig. 3, A and B; and Fig. S1 L). Golgi staining of CA1

pyramidal neurons in the mouse brain revealed comparable spine density but somewhat larger spine sizes (Fig. 3, C and D; and Fig. S1 M). Ultrastructural analysis using electron microscopy further revealed enlarged PSDs in brain slices from F367A mice, quantified by increased PSD length and thickness when compared with synapses from WT mice (Fig. 3, E and F).

We also analyzed the expression and subcellular localizations of key synaptic proteins using biochemical fractionation. Hippocampi from WT and F367A mice were processed into distinct fractions: whole homogenate (Homo), synaptosome-enriched synaptic membrane fraction (Syn), twice Triton-extracted PSD



fraction (PSD), and sarcosyl-extracted core PSD (PSD_{core}). Quantitative analysis of fractionated proteins revealed that while total IQSEC2 expression was reduced in F367A mice, the mutant IQSEC2 was significantly more enriched in the synaptosome and PSD fraction when compared with WT IQSEC2 (Fig. 3, G and H). In parallel, PSD-95, GluN2B, GluA1, and GluA2 were also more enriched in the PSD of F367A mutant mice, further corroborating the mutation's role in promoting excessive AMPAR retention and stabilizing synaptic architecture and consistent with our earlier electrophysiological and dendritic spine morphology data.

Collectively, the above synaptic structural and molecular analysis reveals that the F367A mutation led to enhanced synaptic strengthening, a finding that correlates well with increased basal synaptic transmissions of the mutant mice. Our results further raise the possibility that IQSEC2 at its open conformation plays certain structural roles in addition to its enzymatic role as a GEF.

Ca²⁺-dependent redistribution of IQSEC2 in HeLa cells

To understand how IQSEC2 may respond to Ca²⁺ concentration fluctuation in cells, we expressed WT and F367A mutant of IQSEC2 in HeLa cells and monitored their subcellular distribution changes upon ionomycin-induced Ca²⁺ influx. Mirroring a prior report (Myers et al., 2012), IQSEC2_WT shifted from a diffuse distribution to a discrete puncta pattern following ionomycin treatment. In stark contrast, F367A exhibited a constitutively punctate pattern independent of cellular Ca²⁺ concentrations (Fig. 4, A–D). These results suggest that Ca²⁺ influx disrupts intramolecular coupling between its IQ and Sec7-PH tandem, leading to cellular puncta formation for the open state IQSEC2. The F367A mutant is in the constitutively open conformation and thus not responsive to a cellular Ca²⁺ concentration rise.

Ca²⁺-regulated conformational opening triggers IQSEC2 membrane recruitment

Further confocal imaging analysis showed that IQSEC2 puncta, derived from its open conformation, are attached to plasma membranes (Fig. 4, E and F). Previous studies have shown that the Sec7-PH tandem of IQSECs interacts with negatively charged lipids, orienting the catalytic domain in close apposition to the plasma membranes where ARFs are located (Aizel et al., 2013; Jian et al., 2012; Karandur et al., 2017) (Fig. 4, G and H; and Fig. S2, A-C). Structural analysis of the apo-CaM/IQ/Sec7-PH complex revealed that the negatively charged IQ/apo-CaM obstructs the Sec7-PH tandem from binding to lipid membranes (Fig. 4 H). These findings collectively indicate that the autoinhibited conformation prevents IQSECs from binding to plasma membranes and that Ca²⁺-induced release of the autoinhibition triggers membrane recruitment of IQSECs. To directly validate this model, we assessed IQSEC2's binding to PI(4,5)P2-containing liposomes using a sedimentation-based assay. Titration of the IQ/apo-CaM into the Sec7-PH tandem resulted in a dose-dependent reduction in the lipid membrane-binding capacity of the Sec7-PH tandem (Fig. 4 I).

Multiple functional domains of IQSEC2 are involved in Ca²⁺-induced puncta formation

IQSEC2 is a large multidomain protein containing an N-terminal coiled-coil (CC) domain, an IQ motif, a catalytic Sec7 domain coupled with a membrane-binding PH domain, and a C-terminal PBM (Fig. 4 J). To delineate the roles of each structural element in Ca²⁺-induced membrane puncta formation of IQSEC2, we expressed various domain-truncation mutants in HeLa cells and assessed their puncta formation patterns before and after ionomycin treatment (Fig. 4, J-L).

Similar to the IQSEC2 F367A mutant, deletion of the IQ motif (ΔIQ) led to constitutive cellular puncta formation in cells, as the Sec7-PH tandem in the mutant should be exposed to lipid membrane regardless of Ca²⁺ concentrations (Fig. 4, J-L). We also generated an IQSEC2 mutant (PHmut) in which positively charged residues in the lipid membrane-binding loops of the PH domain were neutralized (residues labeled in Fig. 4 H). The PHmut not only detached the protein from the membrane but also significantly reduced puncta formation following ionomycin treatment, indicating that both the Ca2+-induced conformational opening and lipid membrane binding are important for IQSEC2 to form condensed puncta beneath the plasma membranes. The loop regions connecting the functional domains of IQSEC2 contain several stretches of conserved, intrinsically disordered sequences (Fig. S2 D). Deleting part of the C-terminal loop (\triangle Cter) or removal of all the loops (\triangle Loop) progressively reduced Ca2+-dependent puncta formation of IQSEC2 (Fig. 4, J-L).

Consistent with previous biochemical analysis (Bai et al., 2023), the R359C and A350D mutants of IQSEC2 formed puncta in HeLa cells even under resting conditions, presumably due to the mutation-induced conformational opening (Fig. S2 E). Ionomycin treatment further increased droplet formation by further enhancing conformational opening induced by Ca²⁺-CaM (Bai et al., 2023). In contrast, the Q801P mutant, which exhibits Ca²⁺-induced conformational changes similar to IQSEC2_WT (Bai et al., 2023), was diffusely distributed in the cytosol under resting conditions but formed condensed puncta upon ionomycin treatment (Fig. S2 E).

N-terminal tetramerization is critical for IQSEC2 puncta formation

Deletion of the N-terminal CC domain also dramatically weakened the IQSEC2 puncta formation, although the mutant still displayed a Ca²⁺-dependent puncta formation property (Fig. 4, J–L). Presence of the CC domain is a common feature of PH domain-containing Arf-GEFs, including cytohesin/ARNO, EFA6/PSD, and IQSEC/BRAG families. Within the IQSEC family, IQSEC2 and IQSEC3 possess an N-terminal CC domain (Fig. S2 F), which undergoes concentration-dependent oligomerization (Fig. S2, G–K).

To elucidate the molecular mechanisms underlying oligomer formation, we determined the crystal structure of the IQSEC2 CC domain at 1.77 Å resolution (Table 1). The structure reveals a head-to-head "dimer of dimers" assembly, consisting of two parallel CCs (Fig. 5 A). Detailed structural analysis identified a key tetrameric assembly interface stabilized by four pairs of interchain salt bridges formed between E25 and R18 (Fig. 5 A).



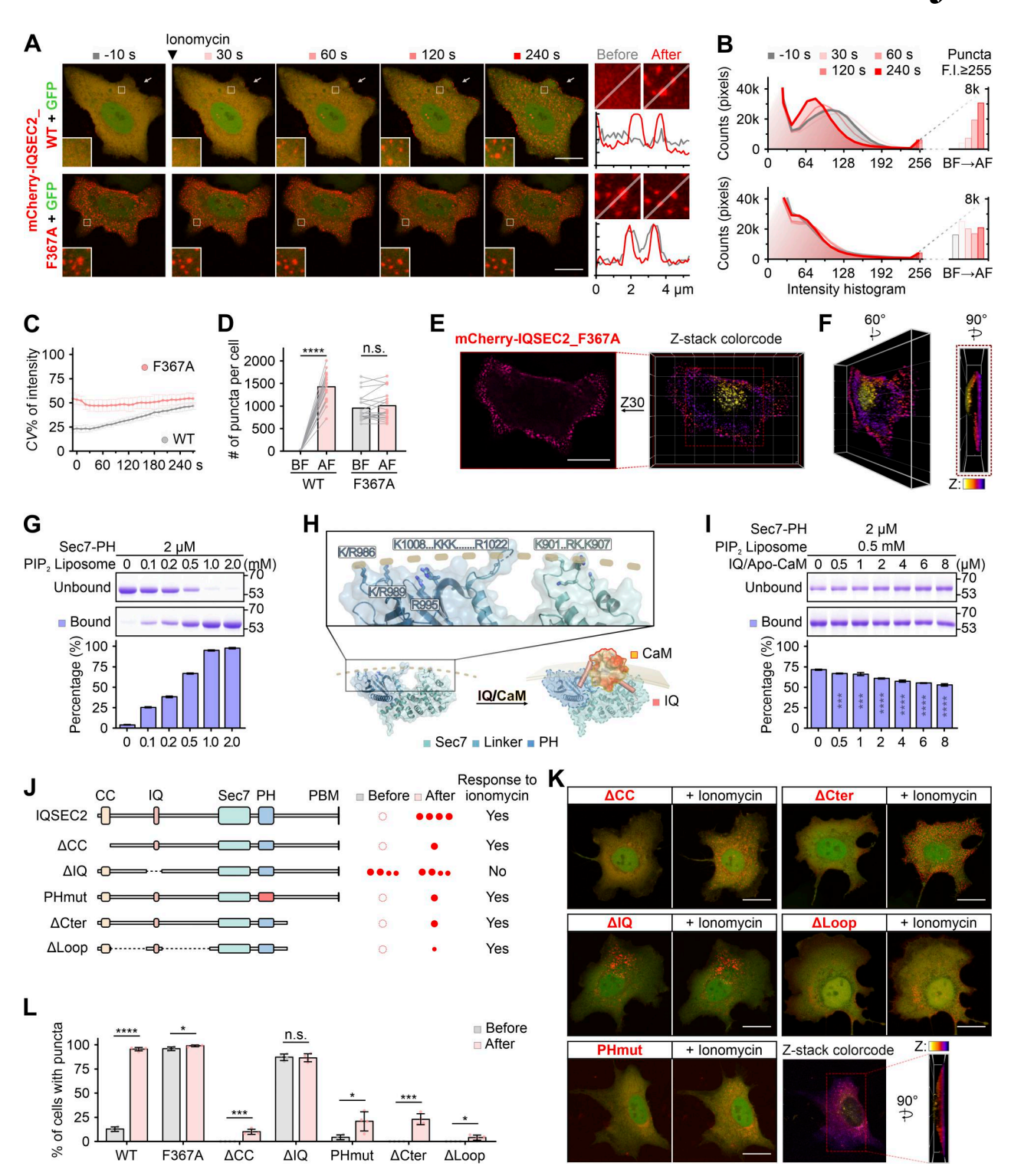


Figure 4. Ca²⁺-regulated allosteric transition of IQSEC2 triggers its membrane recruitment and puncta formation in heterologous cells. (A) Time-lapse imaging showing the formation of puncta in response to calcium influx in HeLa cells expressing mCherry-IQSEC2. Line-scanning plots showing the relative mCherry fluorescent signal distribution before and after ionomycin stimulation in the zoomed-in images. White arrow, membrane-attached puncta. Scale bar, 20 μm. See also Video 1. (B) The mCherry signal intensity profile from time-lapse imaging shows the separation of low-intensity (diffused signal) and high-intensity (puncta) fractions upon ionomycin treatment. Histograms for different times are colored according to labels in A. (C) Time-series plots of the coefficient of variation (CV%) of mCherry fluorescent signal representing mCherry-IQSEC2 puncta formation process after ionomycin treatment in A. 12 regions in each cell were calculated. Data are presented as mean ± SD. (D) Quantification of the puncta number within cells before and after ionomycin treatment. Data were presented as mean ± SD (20 cells from four batches of cultures per group; n.s., not significant; ****P < 0.0001; paired t test). (E) Representative Z-stack color-coded 3D projection and a single-panel image showing membrane-attached mCherry-IQSEC2_F367A puncta in transfected HeLa cells before ionomycin treatment. (F) The 3D reconstructed image viewed at different angles. (G) Co-sedimentation assay showing that the Sec7-PH tandem of IQSEC2 interacts with the PIP₂ liposome (48% POPC, 30% DOPS, 20% DOPE, and 2% PI(4,5)P₂). Data from three different batches of experiments were presented as mean ± SD.



(H) The IQ-bound and negatively charged apo-CaM occludes the PH domain of IQSEC2 from binding to lipid membranes. The membrane-facing surface of Sec7-PH tandem shows exposed positively charged residues. The position of the membrane is indicated. The surface of CaM is colored yellow for hydrophobic residues, blue for positively charged residues, and red for negatively charged residues. (I) IQ/Apo-CaM titration showing it blocks the Sec7-PH tandem from attaching to the PI(4,5)P₂ liposome. Data from three repeated experiments were presented as mean \pm SD (***P < 0.001; ****P < 0.0001; one-way ANOVA). (J) Schematic domain structure and summary of puncta formation in HeLa cells of IQSEC2 and truncation mutants. Dashed circles represent overexpressed mCherry-IQSEC2 proteins diffusely distributed in the cytoplasm. Dots represent the relative puncta number and size before and after ionomycin stimulation. Domain organization is drawn to scale: the N-terminal CC domain, the IQ motif (IQ), the Sec7 and PH tandem, and the C-terminal PBM. (K) Representative images of HeLa cells expressing indicated mCherry-IQSEC2 mutants before and after ionomycin treatment. Color-coded 3D projection and orthogonal view of PHmut demonstrating its detachment from the plasma membranes. Scale bars, 20 μ m. (L) Quantification of the percentage of cells with puncta over the total transfected cells before and after ionomycin treatment. Data from four independent batches of cultures were presented as mean \pm SD (n.s., not significant; *P < 0.005; ***P < 0.001; ****P < 0.0001; unpaired t test). PI(4,5)P₂, phosphatidylinositol 4,5-phosphate. Source data are available for this figure: SourceData F4.

N-terminal truncation or introduction of a charge-reversal mutation (R18E) significantly weakened tetramerization or completely converted IQSEC2_CC into a dimer (Fig. 5 B). Additionally, replacing Leu47 in the hydrophobic core of the CC with Asp (L47D) converted IQSEC2_CC into a clean monomer (Fig. 5 C; and Fig. S2, F, L, and M).

Two de novo in-frame deletions in the CC domain (p.N28del and p.I30del) have been identified as pathogenic IQSEC2 variants (Mignot et al., 2019; Shoubridge et al., 2019). The N28del variant was identified in a female patient with Rett syndrome via exome sequencing (Sajan et al., 2017), and the I30del variant was reported in a male with unexplained epilepsy and ID/developmental delay via gene-targeted sequencing (Zhang et al., 2015). Structural analysis revealed that both N28 and I30 residues are located within the tetramer-forming region of the CC domain (Fig. 5 A). Deletion of either residue alters the heptad repeat register of the CC and thereby destabilizes the folding of the IQSEC2 CC domain (Fig. S2, L and M). Consistently, analytical SEC showed that neither the N28del nor the I30del mutants formed tetramers but instead the mutants shifted toward dimers or even partial dissociation of dimers (Fig. 5 C), highlighting the critical role of these two residues in the higher-order oligomer assembly of IQSEC2_CC.

To investigate the functional impact of the N28del and I30del variants, we examined their influence on Ca²⁺-induced IQSEC2 puncta formation in HeLa cells. Compared with IQSEC2_WT, cells expressing IQSEC2_N28del, IQSEC2_I30del, and the monomeric IQSEC2_L47D exhibited progressively reduced puncta formation (both in percentage of cells forming puncta and signal intensities of the formed puncta) as a function of the degree of tetramer to monomer conversion caused by the mutations (Fig. 5, D-F). These findings may provide a mechanistic explanation for why the N28del and I30del mutations in IQSEC2 may cause brain disorders.

Ca2+-induced phase separation IQSEC2

We performed FRAP assay of IQSEC2 puncta formed in HeLa cells to probe the Ca²⁺-dependent changes in its lateral mobility (Fig. S3, A and B). Before ionomycin treatment, each cell contained very few IQSEC2 puncta. These few IQSEC2 puncta were presumably formed due to the basal cytoplasmic Ca²⁺ concentration fluctuations. Fluorescence signals of IQSEC2 under basal conditions recovered to >50% after photobleaching. After ionomycin treatment, the IQSEC2 exhibited very low recovery, likely due to its attachment to the membrane surface and thus restricting its diffusion.

Careful analysis of Ca²⁺-induced IQSEC2 puncta formation process in cells showed that IQSEC2 first formed small discrete microclusters, which further merged into larger puncta (Fig. 4 A and Video 1). Notably, this fusion process is reversible: upon ionomycin washout, the large IQSEC2 puncta disassemble into a diffused pattern (Myers et al., 2012). Thus, it indicated that this dynamic, Ca²⁺-dependent IQSEC2 puncta formation and dispersion observed in cells may be mediated by Ca²⁺-induced phase separation of the protein.

We next directly tested whether purified IQSEC2 or its various domains may undergo phase separation in vitro. We found that purified recombinant Sec7-PH tandem spontaneously formed spherical, condensed droplets via phase separation in a physiological buffer (Fig. 6 A). These droplets exhibited gradual growth over time, indicative of a dynamic assembly process (Fig. S4 A). However, the concentration required for phase separation to occur (>75 μ M; Fig. 6 A and Fig. S4 B) far exceeds the physiological concentration of IQSEC2 in cells (estimated to be ~10 μ M in synapses [Dosemeci et al., 2007; Lowenthal et al., 2015]). Interestingly, covalently linking the N-terminal CC domain with the Sec7-PH tandem (CC~Sec7PH) dramatically lowered the phase separation threshold to below 5 μ M (Fig. 6 B and Fig. S4 C) due to the CC domain-mediated valency increase of CC~Sec7PH.

To investigate the Ca²⁺-dependent IQSEC2 puncta formation observed in cells, we performed phase separation assays using a purified IQ~Sec7PH chimera of IQSEC2, in which the IQ motif is covalently linked to the Sec7-PH tandem (Bai et al., 2023). In the absence of Ca²⁺, IQ~Sec7PH/apo-CaM showed no signs of condensation even at concentrations up to 50 μ M. In contrast, in the presence of Ca²⁺, the IQ~Sec7PH/CaM complex formed condensed droplets via phase separation with a threshold concentration of ~20 μ M (Fig. 6 C and Fig. S4 D). Strikingly, the F367A mutant of IQ~Sec7PH chimera, which adopts a constitutively open conformation, formed droplets under both Ca²⁺-free and Ca²⁺-saturated conditions (Fig. 6 C and Fig. S4 E).

Unfortunately, attempts to purify IQSEC2 constructs containing both the CC domain and the IQ~Sec7PH boundary were unsuccessful, as the recombinant proteins were expressed in insoluble forms. As an alternative, we employed a SpyTag/SpyCatcher system to generate an IQ~Sec7PH/CaM dimer (Zakeri et al., 2012) (see Fig. 6 D for the scheme and prepared dimeric protein). In the absence of Ca²⁺, this dimer did not form condensed droplets at concentrations as high as 20 μ M (Fig. 6 E



Table 1. Crystallographic data collection and refinement statistics

Data collection	
Space group	P2 ₁ 2 ₁ 2 ₁
Wavelength (Å)	0.97852
Unit cell parameters a, b, and c (Å) α , β , and γ (°)	20.133, 69.842, and 169.327 90
Resolution range (Å)	50-1.77 (1.80-1.77)
No. of unique reflections	23,777 (1,130)
Redundancy	11.1 (10.4)
Ι/σ	23.6 (1.8)
Completeness (%)	96.3 (93.2)
R _{merge} ^a (%)	12.2 (80.7)
CC _{1/2}	0.996 (0.975)
Structure refinement	
Resolution (Å)	1.77
R _{work} ^b (%)	22.03
R _{free} ^c (%)	28.47
RMSD bonds (Å)	0.009
RMSD angles (°)	1.024
Average B factor (Ų)	36.19
No. of atoms	
Protein	1,749
Water	134
B factors (Ų)	
Proteins	35.72
Water	42.30
Ramachandran plot (%)	
Preferred	99.49
Allowed	0.51
Outliers	0

Numbers in parentheses represent the values for the highest-resolution shell.

and Fig. S4 F). Upon Ca^{2+} addition, the dimer rapidly formed droplets at a concentration as low as 1 μ M (Fig. 6 E; and Fig. S4, F and G). These droplets fused into larger ones upon contact (Fig. S4 H), and the protein exhibited dynamic exchange between the condensed and dilute phases, as demonstrated by FRAP analysis (Fig. S4, I and J). Importantly, the addition of EGTA dispersed the formed droplets, indicating reversible and Ca^{2+} -dependent IQSEC2 condensate formation via phase separation (Fig. 6 F). These results demonstrate that IQSEC2 undergoes Ca^{2+} -induced phase separation under physiological conditions (threshold

 \sim 1 μ M, lower than its estimated synaptic abundance), offering a mechanistic explanation to the ionomycin-induced condensate formation observed in cells.

IQSEC2/PSD-95 complex form condensed assembly via phase separation

Previous studies have shown that the C-terminal PBM of IQ-SEC2 interacts with PSD-95, a prominent scaffolding protein in the excitatory PSD (Sakagami et al., 2008) (Fig. S5, A and B). This interaction is critical for the enrichment of IQSEC2 within the PSD. Fluorescence imaging analysis of the mouse CA1 region with genetically tagged endogenous mScarlet-IQSEC2 (Bai et al., 2023) and PSD-95 immunostaining showed that the two proteins are colocalized (Fig. 7 A). We further co-expressed mCherry-IQSEC2 and GFP-PSD-95 in HeLa cells. Under the resting condition, both PSD-95 and IQSEC2 were largely diffusely distributed in the cytosol. In contrast, following ionomycin treatment, PSD-95 partitioned into the mCherry-IQSEC2 condensates beneath the plasma membrane (Fig. 7 B). Unlike the very low recovery of mCherry-IQSEC2 after ionomycin treatment during FRAP analysis, signals of PSD-95 were recovered after photobleaching both before and after ionomycin treatment (Fig. S3, C and D). The signal recovery rate and level of PSD-95 were slower and lower after ionomycin treatment, presumably because the IQSEC2/PSD-95 condensate is more stable, and the concentration of PSD-95 in the dilute phase is lower under high cellular Ca²⁺ conditions.

Importantly, when mCherry-IQSEC2_ Δ PBM, which lacks the PBM and cannot bind PSD-95, was co-expressed with GFP-PSD-95, PSD-95 remained diffused in the cytosol even after ionomycin treatment, whereas mCherry-IQSEC2_ Δ PBM formed condensates (Fig. 7 B). These findings highlight the essential role of the PBM in mediating the specific interaction between IQSEC2 and PSD-95 and the recruitment of PSD-95 to IQSEC2 condensates in heterologous cells.

IQSEC1, another IQSEC family member enriched in the excitatory PSD (Lowenthal et al., 2015; Scholz et al., 2010), also possesses a PBM sequence similar to IQSEC2 (Fig. S5 A). ITC-based assay showed that IQSEC1_PBM also binds to PSD-95 (Fig. S5 B). Co-expression experiment confirmed that PSD-95 is recruited to IQSEC1 condensates in a Ca²⁺-dependent manner (Fig. S5 C). In contrast, the inhibitory synapse-specific protein IQSEC3 displayed no detectable binding to PSD-95 (Fig. S5 B). When expressed in HeLa cells, IQSEC3 also formed distinct puncta following ionomycin treatment, but such IQSEC3 puncta did not recruit PSD-95 (Fig. S5 C).

To investigate the phase separation behavior of the IQSEC2/PSD-95 complex in vitro, we conducted experiments using purified IQ~Sec7PH~PBM/CaM and PSD-95. In the absence of Ca²+, minimal droplet formation was observed when both proteins were mixed at a 1:1 M ratio and each at 20 μ M (Fig. 7 C). This suggests that without Ca²+, the interaction between IQSEC2 and PSD-95 is not sufficient to drive significant phase separation and droplet formation. Remarkably, upon Ca²+ addition, prominent co-condensation of IQSEC2 with PSD-95 was induced at a protein concentration as low as 5 μ M (Fig. 7 C and Fig. S5 D).

 $^{{}^{}a}R_{merge} = \Sigma |I_i - \langle 1 \rangle |/\Sigma I_i$, where I_i is the intensity of measured reflection and $\langle I \rangle$ is the mean intensity of all symmetry-related reflections.

 $^{{}^{}b}R_{work} = \Sigma_{W}||F_{calc}| - |F_{obs}||/\Sigma|F_{obs}|$, where F_{obs} and F_{calc} are observed and calculated structure factors. W is working dataset of about 95% of the total unique reflections randomly chosen and used for refinement.

 $^{{}^}cR_{free} = \Sigma_T ||F_{calc}| - |F_{obs}||/\Sigma |F_{obs}|$, where T is a test dataset of about 5% of the total unique reflections randomly chosen and set aside prior to refinement.



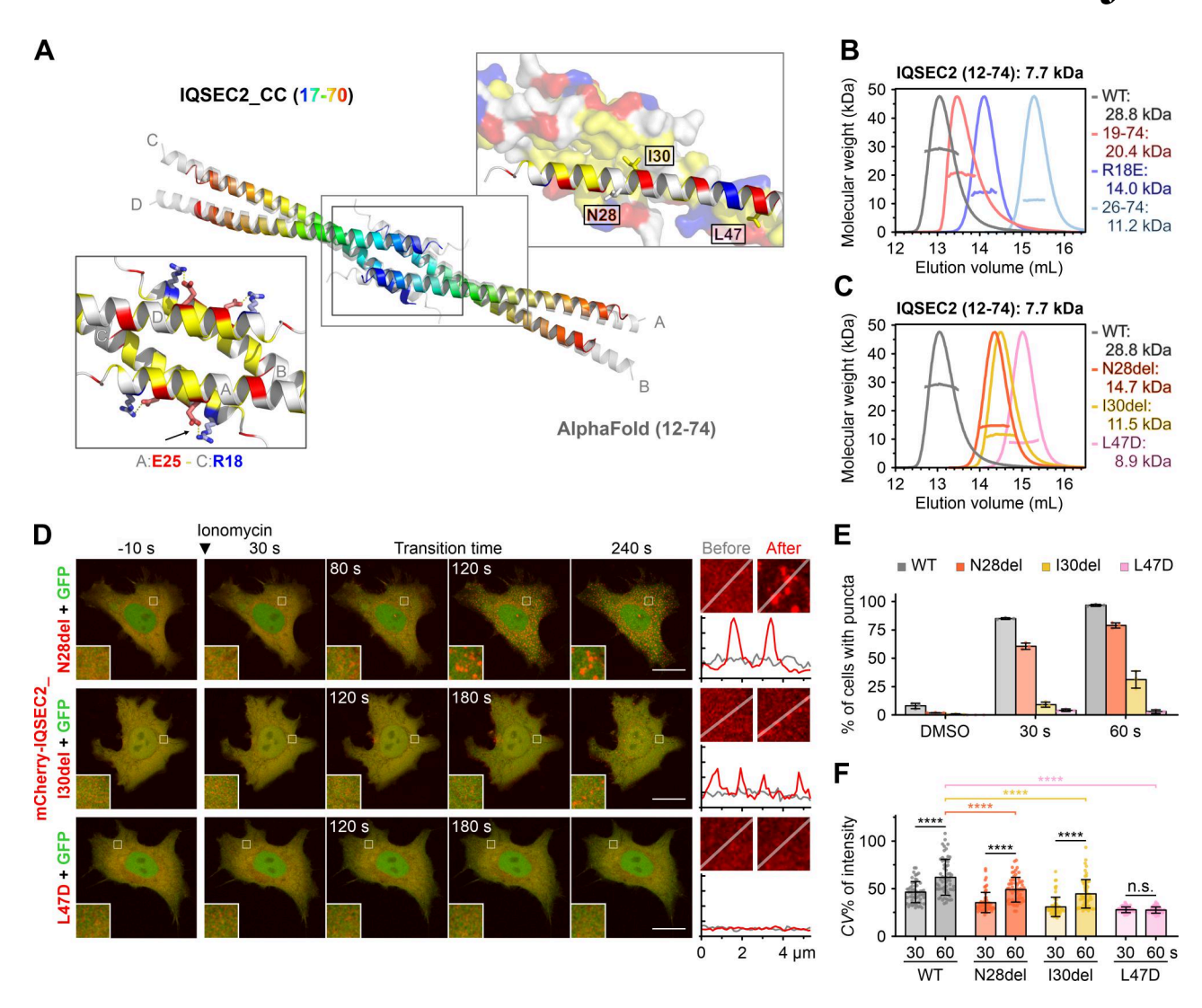


Figure 5. **N-terminal CC domain tetramerization is essential for IQSEC2 puncta formation. (A)** Crystal structure of the IQSEC2 N-terminal CC tetramer (rainbow) and superposition of an AlphaFold predicted model (gray), (r.m.s. deviation of 1.127 Å). The four CC chains (colored blue to red in an N- to C-terminal direction) are arranged in a head-to-head dimer of dimers assembly of two parallel CCs. The head-to-head assembly interface is stabilized by four pairs of salt bridges between E25 and R18 from neighboring dimers and is supported by surrounding hydrophobic interactions. **(B)** SEC-MALS analysis of the IQSEC2_CC (aa 12–74, calculated MW 7.7 kDa) reveals that it exists as a 28.8-kDa tetramer (theoretical: 30.8 kDa), whereas the N-terminal truncation (aa 26–74, calculated MW 6.2 kDa) and R18E mutation each formed a dimer. Another N-terminal truncation mutant (aa 19–74, calculated MW 7.0 kDa) eluted with a molecular mass between dimer and tetramer. Fitted molecular masses are plotted across elution peaks. **(C)** SEC-MALS analysis of two pathogenic variants (N28del and I30del) and the L47D point mutation, each in the IQSEC2_CC (12–74) parental construct. **(D)** Time-lapse imaging of HeLa cells expressing mutants of mCherry-IQSEC2 and treated with ionomycin for the indicated time. Line-scanning plots showing the relative mCherry fluorescent signal distribution before and after ionomycin stimulation in the zoomed-in images. Scale bar, 20 µm. **(E)** Quantification of the percentage of transfected cells exhibiting puncta after treatment with DMSO or ionomycin for 30 and 60 s. Data from four independent batches of cultures were presented as mean ± SD. **(F)** Quantification of the coefficient of variation (CV%) of mCherry fluorescent signal representing mCherry-IQSEC2 puncta formation after 30 and 60 s of ionomycin treatment. Data were presented as mean ± SD (60 cells from four batches of cultures per group; n.s., not significant; ****P < 0.0001; unpaired t test between 30 and 60 s; one-way ANOVA among WT and mutants).

Individually, neither protein formed droplets regardless of Ca²+ presence (Fig. S5 E). And the direct interaction between IQSEC2_PBM and PSD-95 is essential for the Ca²+-induced phase separation of the complex (Fig. S5 F). The presence of PSD-95 reduced the threshold concentration from 20 to 5 μM (compare Fig. S5 D with Fig. S4 D). We anticipate that the full-length IQSEC2 containing the N-terminal CC domain and the intrinsically disordered regions will have an even lower threshold concentration to co-phase separate with PSD-95.

IQSEC2 promotes PSD condensate formation via binding to PSD-95

To gain insights into whether IQSEC2 could be recruited to the PSD system via binding to PSD-95 (Fig. 7 D) and how the Ca²⁺-induced phase separation of IQSEC2 might influence the PSD assembly, we reconstituted PSD condensates containing four major scaffold proteins, namely PSD-95, GKAP, Shank3, and Homer3, as previously reported (Zeng et al., 2018). Our experiments demonstrated that $IQ\sim Sec7PH\sim PBM/CaM$ was



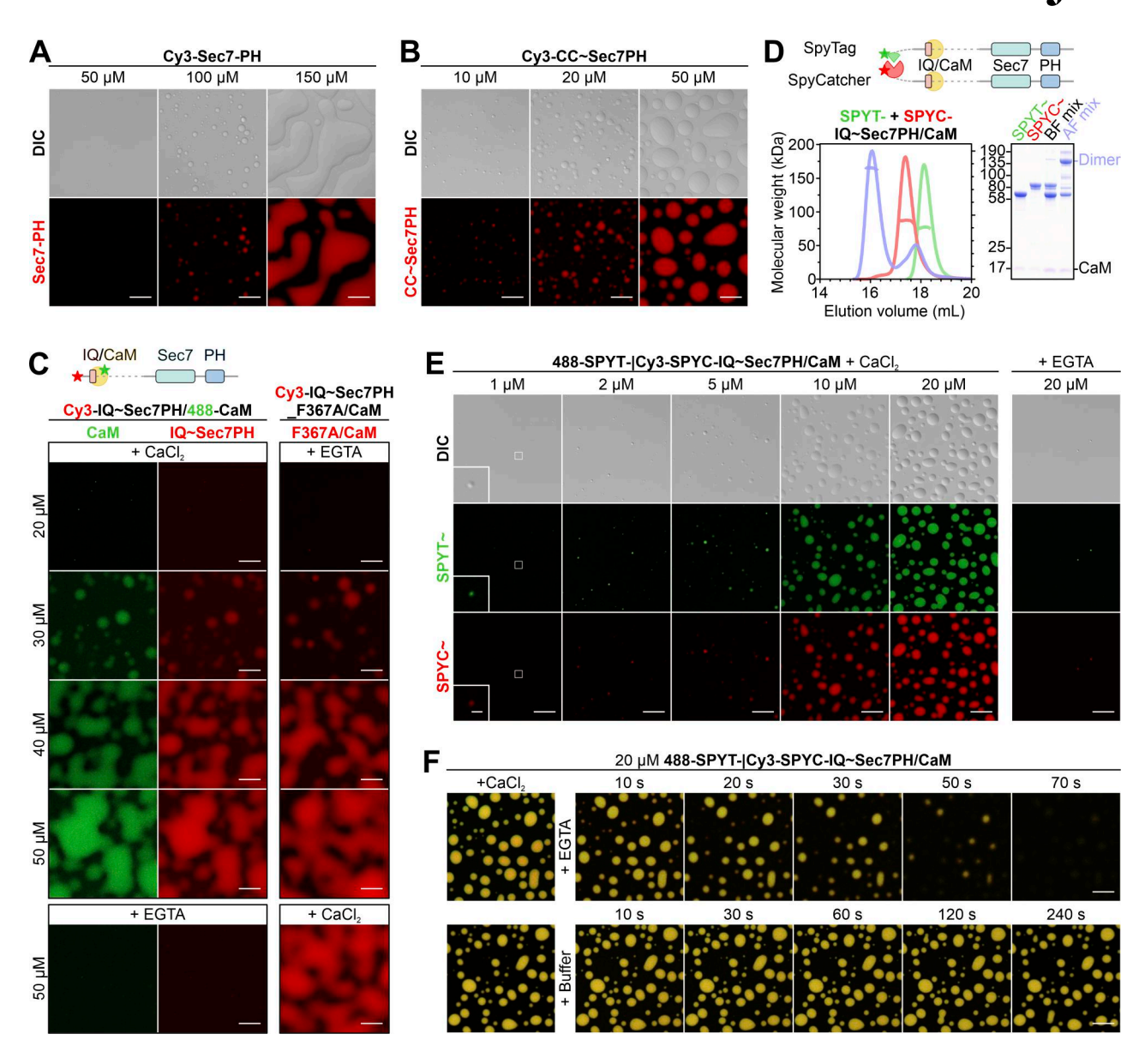


Figure 6. Ca²⁺-induced phase separation of IQSEC2. (A and B) Fluorescence images showing that the Sec7-PH protein alone undergoes phase separation at high concentrations and its N-terminal tetramerization promotes the condensate formation. (C) Fluorescence images showing that the IQ~Sec7PH/CaM complex undergoes Ca²⁺-induced phase separation. Note that the F367A mutant, which carries a missense mutation that disrupts the CaM/IQ/Sec7-PH coupling, exhibits a concentration-dependent condensation behavior in the absence of Ca²⁺, similar to the WT protein in the presence of Ca²⁺. Scale bars, 10 μm. (D) SEC-MALS analysis and representative SDS-PAGE showing that the SPYT-IQ~Sec7PH/CaM and SPYC-IQ~Sec7PH/CaM form a stable heterodimer in solution. (E) Fluorescence images showing that Ca²⁺ induces phase separation of SPYT|SPYC-IQ~Sec7PH/CaM heterodimer at a low protein concentration. Scale bar, 10 μm. Scale bar for the zoomed-in images, 1 μm. (F) Time-lapse imaging showing that the Ca²⁺-induced condensate formation of IQSEC2 can be reversed by EGTA. Scale bar, 10 μm. Source data are available for this figure: SourceData F6.

indeed co-sedimented with PSD components, and its presence significantly promoted the enrichment of PSD-95 within the PSD condensates. However, the lower-layer PSD components (GKAP, Shank3, and Homer3) showed only minor changes in their enrichment (Fig. 7 E; and Fig. S5, G and H). This selective incorporation requires the IQSEC2-PBM/PSD-95 interaction, as evidenced by abolished recruitment of IQSEC2 when either PSD-95 was omitted or the PBM was deleted (Fig. S5, I and J).

Ca²⁺ stimulation further amplified condensate formation, driving synergistic enrichment of both IQSEC2 and PSD-95 (Fig. 7 E; and Fig. S5, G and H). These findings collectively

indicate that IQSEC2's phase separation could reorganize the PSD in a Ca²+-dependent manner, and this scaffolding function operates independently of its GEF activity. The specific spatial enrichment—particularly as observed in the constitutively conformationally open F367A mutant, which shows an enhanced PSDcore accumulation despite its lower overall expression (Fig. 3)—suggests a feedforward mechanism where phase separation causes further local concentration of IQSEC2 as well as other PSD proteins. Thus, IQSEC2 may serve as a Ca²+-induced amplifier of synaptic structural organizations both as an enzyme with GEF activities and as a scaffold protein.



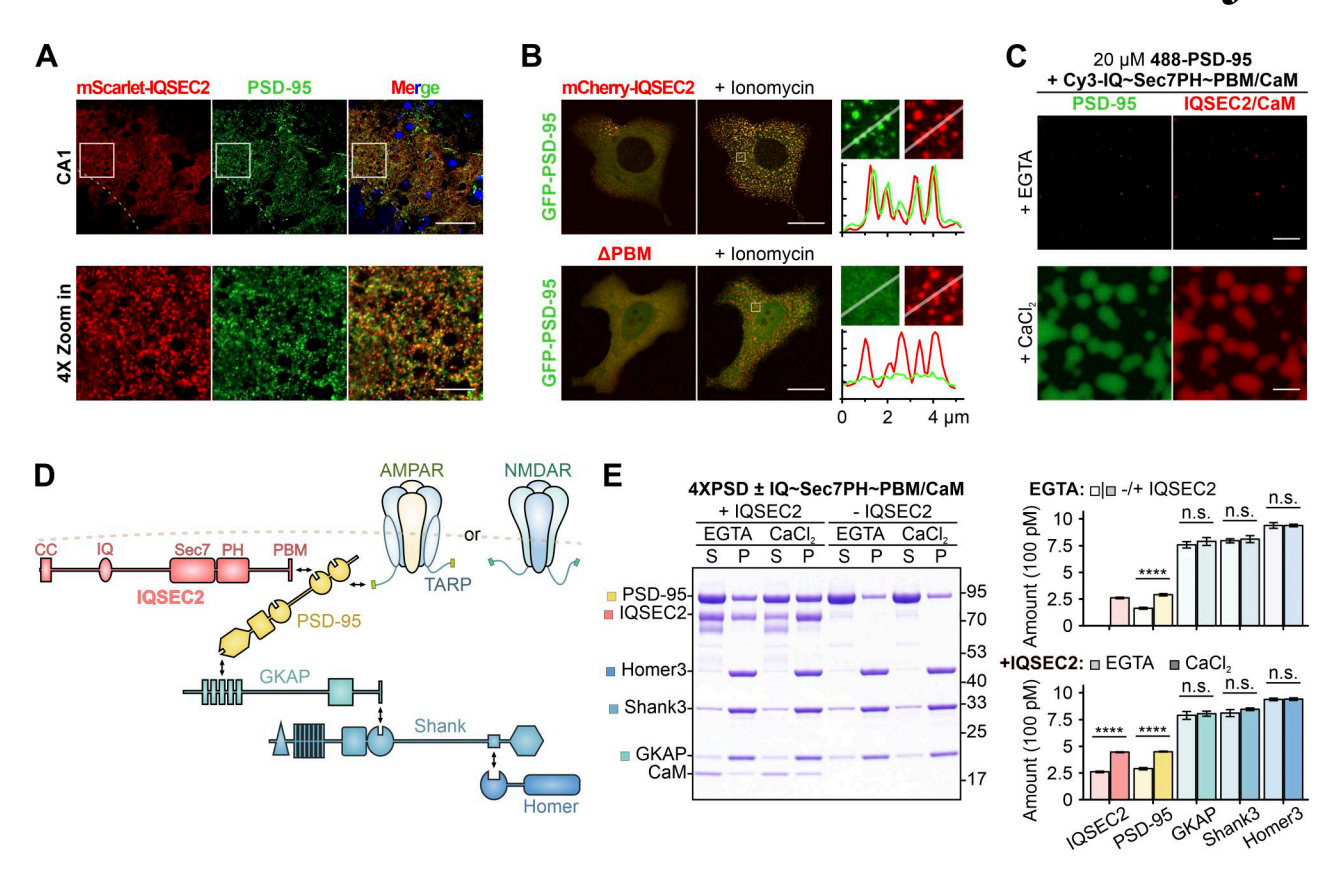


Figure 7. **IQSEC2 phase separation facilitates PSD-95 enrichment in reconstituted condensates. (A)** Fluorescence images of a hippocampal CA1 region immunostained with PSD-95 from mScarlet-Iqsec2-tagged adult mouse brains. Scale bar, 40 μm. Scale bar for the zoomed-in images, 10 μm. **(B)** Co-expression of mCherry-IQSEC2 with GFP-PSD-95 in HeLa cells led to puncta formation, with the two proteins colocalized together in each punctum. Upon ionomycin stimulation, the phase separation of IQSEC2 promoted their co-condensation. Deletion of the C-terminal PBM in IQSEC2 abolished Ca^{2+} -induced recruitment of PSD-95 to the IQSEC2 droplets. Fluorescence intensity line-scanning plots show that IQSEC2 and PSD-95 are concentrated and colocalized together in the bright puncta shown in the zoomed-in images. Scale bar, 20 μm. **(C)** Fluorescence images showing that IQ~Sec7PH~PBM/CaM and PSD-95 underwent Ca^{2+} -induced phase separation. Scale bar, 10 μm. **(D)** Domain architecture and interaction network of the major PSD proteins. **(E)** Representative SDS-PAGE of sedimentation experiments (left panel) and quantification of protein amounts in the pellet (right panel), showing that IQSEC2 promotes PSD-95 integration into the PSD condensates, and Ca^{2+} further enhanced IQSEC2 and PSD-95 enrichment in the PSD condensates. The input concentration of each component was 10 μM. Data from three repeated experiments were presented as mean \pm SD (n.s., not significant; ****P < 0.0001; unpaired t test). Source data are available for this figure: SourceData F7.

Discussion

We previously established that IQSEC2 operates via Ca²⁺-dependent release of autoinhibition, explaining its genotype-phenotype relationships for a large fraction of *IQSEC2* mutations found in patients with neurodevelopmental disorders (Bai et al., 2023). In this study, we advance this understanding by revealing how Ca²⁺-induced conformational changes and consequent phase separation of IQSEC2 regulate its synaptic function through two distinct mechanisms: namely, IQSEC2 acting as an enzyme (i.e., as a GEF for ARFs) and as a scaffold protein for orchestrating PSD condensates.

Previous reports have shown that IQSEC2 dosage directly modulates basal synaptic strength, with reduced levels of the protein impairing synaptic transmission and elevated levels enhancing it (Brown et al., 2016; Hinze et al., 2017). Building on our findings that IQSEC2 promotes the PSD condensate formation through phase separation, we propose that this dosage-dependent function in synaptic transmissions is related to IQSEC2's capacity to co-condense with PSD-95. This model suggests that IQSEC2 can play structural roles in modulating synaptic plasticity.

Thus, Ca2+ signals bidirectionally regulate IQSEC2's dual function. On one hand, Ca2+ activates IQSEC2's catalytic GEF domain, driving ARF6-mediated AMPAR internalization to weaken synapses during LTD. On the other hand, Ca²⁺ promotes IQSEC2-PSD-95 co-condensation, enhancing the PSD condensate formation and hence synaptic enlargements. The dual regulation of IQSEC2 by Ca2+ signals during synaptic plasticity likely reflects differential spatiotemporal Ca²⁺ dynamics in LTD versus LTP. Moderate and low-frequency Ca2+ influx via NMDAR activation during LTD might preferentially trigger localized activation of IQSEC2's GEF domain, driving ARF6mediated AMPAR endocytosis without triggering widespread condensation of the enzyme. Conversely, sustained Ca²⁺ influx during LTP could cause prolonged conformational opening of IQSEC2, leading to its scaffolding roles in promoting the PSD expansion and synaptic strengthening via phase separation. One limitation of the current study is that we did not directly test synaptic activity-dependent localization and mobility changes as well as material properties of IQSEC2 in the PSD. Future studies using knock-in mice models and advanced imaging experiments

Journal of Cell Biology



are needed to definitively establish the dynamics of endogenous IQSEC2 condensation during synaptic plasticity. We anticipate that Ca^{2+} -dependent incorporation of IQSEC2 into PSD may further increase the rigidity of the soft glass-like PSD condensate (Jia et al., 2025).

Synaptic PSDs harbor diverse regulatory enzymes, including various small GTPase GAPs and GEFs, as well as CaMKII. Prior studies showed that synaptic activation can promote synapse formation by Ca2+-CaMKII-mediated dispersion of a negative PSD regulator SynGAP, which is a GAP for Ras/Rap (Araki et al., 2015; Zeng et al., 2016). Interestingly, SynGAP, also highly abundant in synapses, plays both enzymatic and structural roles in regulating synaptic plasticity. As a GAP, SynGAP can regulate synaptic actin cytoskeletal dynamics for synaptic plasticity (Araki et al., 2015; Zeng et al., 2016). As a scaffold protein, SynGAP binds to PDZ domains of PSD-95 and thus antagonizes the interaction between AMPARs and PSD-95 (Araki et al., 2024). CaMKII is the most abundant protein in the synapse. This master Ca2+ signal decoder also functions both as an enzyme and as a scaffold protein in regulating synaptic plasticity. Ca²⁺-mediated CaMKII activation and subsequent autophosphorylation of the kinase are essential for synaptic LTP (Chen et al., 2024; Tullis et al., 2023). On the other hand, the direct binding of CaMKII to the GluN2B subunit of NMDAR is also required for synaptic plasticities (Chen et al., 2024; Halt et al., 2012; Incontro et al., 2018). It appears that simultaneously functioning as enzymes and scaffold proteins is a common property for these and possibly other enzymes abundantly present in synapses (Wu et al., 2025).

By demonstrating that synaptic strength and plasticity may be modulated by Ca²⁺-dependent phase separation, we provide a framework to explain how mutations in IQSEC2 may affect synaptic structure and functions. Future studies should explore whether aberrant phase separation represents a common pathological mechanism in neurodevelopmental disorders and whether modulating condensate dynamics (e.g., via Ca²⁺ signaling or pharmacological targeting of conformational states) can restore synaptic plasticity. Additionally, investigating how IQSEC2 cooperates with other GTPase regulators in modulating the PSD organization will deepen our understanding of synaptic dysregulation in neurodevelopmental disorders.

Materials and methods

Animals

All experimental procedures were conducted following protocols approved by the Animal Ethics Committee at the Hong Kong University of Science and Technology and the Institutional Animal Care and Use Committee of the animal core facility at Huazhong University of Science and Technology, Wuhan, China. Mice were housed in groups of three to five mice/cage under a 12-h light-dark cycle (lighting from 8:00–20:00) with food and water ad libitum, at a consistent ambient temperature (21 ± 1°C) and humidity (50 ± 5%). All tests were performed during the light phase. The mice were handled daily by experimenters for at least 3 days and were then transferred to the testing room for 1-h

acclimation before starting the experiments. Hemizygous and WT littermate males of the single line generated by heterozygous breeding were used as mutant and control mice, respectively, throughout this study. Mice were randomly allocated to different experimental groups. All behaviors were scored by experimenters who were blinded to the genotypes.

Generation of Igsec2 mutant mice

The N-terminal mScarlet-tagged *Iqsec*2 knock-in mice were generated in a previous study (Bai et al., 2023) through spermlike stem cell-mediated semi-cloning technology (Yang et al., 2012; Zhong et al., 2015). IQSEC2 F367A mice were generated by the CRISPR-Cas9-mediated Extreme Genome Editing system (Beijing Biocytogen). Cas9-gRNA target sequences were designed for the regions on exon 3-4 to promote DNA breaks and homologous recombination. The *in vitro*-transcribed Cas9 mRNA, gRNA, and the oligo donors carrying the desired mutation (*p.F367A*, *c.T1099G*, and *T1100C*) were co-injected into fertilized mouse eggs. Primers used for genotyping were as follows: (*Iqsec*2 F367A-F: 5'-AGCCTGTCATGACTTCCAGCAGTT-3'; F367A-R: 5'-TAAGGG AGGCCCCGTTCAAGC-3').

Electrophysiology

Male mice aged 60 ± 2 days were deeply anesthetized (e.g., 3-5%isoflurane induction until loss of reflexes), followed by rapid decapitation. The brains were rapidly removed, and the hippocampal slices (VT1200S; Leica) were immediately prepared in ice-cold slicing artificial cerebrospinal fluid (ACSF) (in mM: 120 choline chloride, 26 NaHCO₃, 25 D-glucose, 5 Na-ascorbate, 7 MgCl₂, 3 Na-pyruvate, 2.5 KCl, 1.25 NaH₂PO₄, and 0.5 CaCl₂ at pH 7.4, with osmolarity at 305 mOsm) saturated with 95% $O_2/5\%$ CO₂ (1–2 liters/min). 300-µm-thick coronal sections were then transferred to a recovery chamber filled with recording ACSF (in mM: 124 NaCl, 3 KCl, 26 NaHCO₃, 1.2 MgCl₂, 1.25 NaH₂PO₄2H₂O, 10 C₆H₁₂O₆, and 2 CaCl₂ at pH 7.4, 95% O₂/5% CO₂, and 305 mOsm) and incubated at 34°C for 30 min, followed by room temperature (22°C) for 60 min. A slice was transferred to a recording chamber, which was continuously perfused with oxygenated ACSF (2 ml/min) at 22°C.

For whole-cell patch-clamp recordings from the CA1 pyramidal cells, hippocampal slices were visualized using infrared (IR) differential interference contrast (DIC) microscopy (C2400-07E; Hamamatsu optics). Resting membrane potentials were measured immediately after the breakthrough. Recordings were considered stable if access resistance (Ra) remained <20 M Ω throughout the experiment; recordings with Ra >25 M Ω were discarded. The EPSCs were evoked by bipolar tungsten electrodes recorded with Axopatch 200B amplifiers and monitored by computer using pClamp11 at 31.5°C in the presence of 10 µM bicuculline. The sEPSC were recorded using an internal solution containing 140 mM potassium gluconate, 10 mM HEPES, 2 mM NaCl, 0.2 mM EGTA, 2 mM Mg²⁺ATP, 0.3 mM NaGTP, and an external solution containing 10 µM bicuculline. The mEPSC were recorded under the same conditions as sEPSC with the additional presence of 1 µM tetrodotoxin. The row electrophysiological data were collected at 10 kHz, filtered with a lowpass filter at 2 kHz, and analyzed using ClampFit 10.2 software



(Molecular Devices) with template matching at a threshold of 5 pA.

To specifically isolate and quantify AMPAR- and NMDARmediated currents, recordings were conducted at defined holding potentials using submaximal stimulation and specialized intracellular solutions. Recordings used a stimulus intensity eliciting 50% or 70% of the maximal AMPAR-EPSC response to avoid saturation. For isolation of receptor-specific currents, a cesium chloride-based internal solution was used to record AMPAR-mediated EPSCs as inward currents at -70 mV clamping potential, while NMDAR-mediated EPSCs were recorded as outward currents at +40 mV clamping potential. The AMPAR/ NMDAR current ratio was calculated from averaged responses over consecutive periods. Evoked EPSC amplitudes were derived from the mean of 12 consecutive responses. NMDAR-mediated currents were quantified at a 50-ms poststimulation time point to avoid contamination by AMPAR-mediated currents. Synaptic currents were evoked by extracellular stimulation pulses (100 µs duration, 20-200 µA intensity, and 0.05 Hz frequency) delivered via concentric bipolar stimulating electrodes using a twisted pair of Formvar-insulated nichrome wires. GABAergic inhibitory postsynaptic currents were isolated by perfusing slices with ACSF containing 20 µmol/l 6-cyano-7-nitroquinoxaline-2,3-dione and 50 μmol/l D-(-)-2-amino-5-phosphonovaleric acid, with recordings performed at -70 mV holding potential. EPSCs were recorded in ACSF containing 10 µmol/l bicuculline to block GABAA receptors. All responses were filtered at 2 kHz, digitized at 10-20 kHz, and representative traces represent averages of 10 consecutive responses.

The standard extracellular recording was used to monitor field EPSPs in the stratum radiatum of the CA1 area of the hippocampal slices in response to the Schaffer-collateral afferent stimulation. Both recording and stimulating electrodes were glass patch electrodes filled with ACSF and with a Ra of 3-5 M Ω . Recordings were made with an Axoclamp 2B amplifier (Molecular Devices), and signals were further processed (100× amplification, 5 kHz low pass filter) using a Brownlee model 440 signal processor (Brownlee, Inc.). Data were monitored online, and EPSP slopes were measured by taking the slope of the rising phase between 5 and 95% and analyzed offline using Win LTP software, as described before (Li et al., 2022). EPSPs were evoked at a frequency of 0.1 Hz. After a 10-min baseline, LTP was induced using two trains of 100 Hz stimulation (1-s duration) separated by a 10-s intertrain interval. Stimulation intensity during the baseline was set to ~35% of the maximal synaptic response. Data were gathered from recordings made from one to three slices per mouse brain and are expressed as the mean ± SD of all the slices.

Behavioral analyses

Home cage behaviors

Individual male mice at 120 ± 5 days old of age were monitored in PhenoTyper home cages ($40 \times 40 \times 40$ cm; Noldus) equipped with IR beams and video tracking. Mice had *ad libitum* access to food and water. After 24-h habituation, locomotion activity and spontaneous behaviors were automatically analyzed by Etho-Vision XT (Noldus) over 24 h.

Open-field test

Following a 60-min acclimation period in the testing room, male mice at 120 ± 5 days old of age were placed facing the wall of an open-field arena ($50 \times 50 \times 38$ cm) and allowed to explore freely for 5 min. Locomotor activity and time spent in the center were analyzed by EthoVision XT (Noldus) as measures of exploratory and anxiety-like behaviors.

Elevated plus maze test

The apparatus used for the elevated plus maze test is 50 cm above the floor, comprising two open arms (28×6 cm, with 0.5-cm tall/wide ledges) across from each other and perpendicular to two closed arms (28×6 cm, with 15×0.5 -cm tall/wide walls) with a center platform (6×6 cm). Mice were placed in the center area, facing an open arm, and allowed to explore freely for 5 min. Their movements were recorded using an overhead camera and analyzed with EthoVision XT (Noldus). Anxiety-like behavior was assessed by analyzing the percentage of time spent in open arms.

Morris water maze

The water maze pool (120 cm in diameter; Chengdu Taimeng Technology) was filled with water at 23 ± 0.5°C, and an escape platform (8 cm in diameter) was submerged 1 cm below the surface of the water during training. Titanium dioxide was dissolved in the water to obscure the submerged platform. Four different graphic patterns were marked on the wall to offer navigation cues for mice to locate the hidden platform. The training session lasted for 6 days. On the first day of training, mice were allowed to find the hidden platform within 90 s and to have 30 s to rest on the platform. If a mouse failed to find the platform within 90 s, it was gently guided to the platform and allowed to remain there for an additional 30 s. Each mouse was trained four times daily with 60-min intervals between successive training sessions, in which the mouse was released from randomized release points in four quadrants of the pool, ensuring balanced exposure to different starting locations across trials. On day 8 (probe test), the platform was removed for probe tests, and mice were placed into the pool in the quadrant opposite the previous platform location and allowed to assess spatial memory retention. Mice were allowed to swim for 90 s, and the time spent in the target quadrant and the number of platform crossings were recorded. Their movements were recorded using an overhead camera and analyzed with EthoVision XT (Noldus).

Monoclonal antibody discovery and purification

An antibody against IQSEC2 was made against a His $_6$ fusion protein encoding aa residues 247–584 of human IQSEC2. Mice were primed and boosted with 50 μ g 1 mg/ml purified antigen protein mixed with 50 μ l Magic Mouse Adjuvant (# CDN-A001; Creative Diagnostics) following the supplier's instructions.

Mouse single cells that secrete the desired antibody were identified by the fluorescent foci assay (Clargo et al., 2014). Briefly, splenocytes from immunized mice were mixed with Ni-NTA beads (88831; Thermo Fisher Scientific) coated with His6-tagged antigen and secondary antibody with Alexa Fluor 488



(A11017; Thermo Fisher Scientific). The mixture was plated in a 6-well plate and incubated at 37°C for 2 h. Fluorescence-positive single cells were identified, picked, and transferred to a PCR tube containing 7.21 μ l lysis buffer containing dT 20mer 2 μ M (51-01-15-01; Integrated DNA Technologies), Triton X-100 0.04% (28314; Thermo Fisher Scientific), and RNaseOUT 14U (10777019; Thermo Fisher Scientific) by using CellCelector (ALS GmbH). Single cells in buffer were stored at -80° C for further processing.

Variable regions of the mouse antibody heavy and kappa chains were cloned according to the reference (Meyer et al., 2019) with modification. After thawing single cells, templateswitching reverse transcription was performed by using SMARTScribe Reverse Transcriptase 5 U/µl (639538; Takara) according to the supplier's instructions. The template-switching oligo is 5'-AAGCAGTGGTATCAACGCAGAGTACGCRGRGRG-3'. Variable regions of mouse antibodies were amplified from the reverse transcription products by using PCRs with forward primer (5'-GTTACAGATCCAAGCTGTGACCAAGCAGTGGTA TCAACGCAGAGT-3') pairing with reverse primer mixture for heavy chain (Ighg1: 5'-GTCACTGTCACTGGCTCAGGGAAA TAG-3', Ighg2b: 5'-GTCACAGTCACTGACTCAGGGAAGTAG-3', Ighg2c: 5'-GTCAAGGTCACTGGCTCAGGGAAATAA-3', and Ighg3: 5'-TTTACAGTTACCGGCTCAGGGAAGTAG-3') or reverse primer for κ chain (5'-GTTCAAGAAGCACACGACTGA GGCAC-3'), respectively. Amplification products were inserted into plasmid vectors containing promoter, constant domain, and polyA signaling using NEBuilder HiFi DNA Assembly (E2621X). Paired heavy and κ chain plasmids were co-transfected into Expi293F cells cultured in Expi293 Expression medium (Cat#A1435102; Thermo Fisher Scientific) using ExpiFectamine 293 Transfection Kit (Cat# A14524; Thermo Fisher Scientific). Culture media containing antibodies were purified by using Protein G HP SpinTrap (28903134; Cytiva).

Plasmid constructs

The full-length cDNAs encoding human IQSEC1 (GenBank accession no. NM_001134382), IQSEC2 (GenBank accession no. NM_001111125), and IQSEC3 (GenBank accession no. NM_001170738) were synthesized by YouBio. All truncations and mutations used in this study were generated by the standard PCR-based methods. For protein purification, PCR products were inserted into modified pET vectors with an N-terminal His₆- or TRX-His₆-tag followed by an HRV-3C protease cutting site (pET.M3C/pET.32M3C). Constructs encoding the IQ motif were cloned into pET.32M3C vectors together with human CaM (GenBank accession no. NM_005184) for co-expression. For protein expression in heterologous cells, PCR products were cloned into modified pEGFP-C3 vectors. All constructs were verified by DNA sequencing.

Cell culture and ionomycin treatment

HeLa cells (from ATCC) were cultured in DMEM media supported by 10% fetal bovine serum, maintained at 37°C with 5% CO_2 . The cells were transfected after 24-h plating at ~40% confluency using a ViaFect transfection kit (Cat# E4982; Promega). 6–8 h after transfection, images were captured on a Leica SP8 confocal microscope. Images were taken right before and

after ionomycin treatment (Cat# I24222; Invitrogen; dissolved at 5 mM in DMSO and diluted to the final concentration of 5 μ M in DMEM) in 5 min at 10 s/frame. The 3D reconstitutions were done with ImageJ.

Primary cultured mouse neurons

Timed pregnant mice generated by heterozygous breeding of IQSEC2 F367A mice were dissected at embryonic day 16.5. Cortex tissue was collected for genotyping. Hippocampal cells were plated onto glass coverslips coated with 1 mg/ml Poly-D-Lysine (Sigma-Aldrich) at a density of 120–150 K/well (of a 12-well plate) and grown in Neurobasal Medium (Gibco) supplemented with 2% B-27 (Gibco), 2 mM GlutaMAX (Thermo Fisher Scientific), penicillin-streptomycin (100 U/ml; Thermo Fisher Scientific), and 5% fetal bovine serum (HyClone). Cells were swapped to serum-free media (as above but lacking serum) at DIV1, fed with media containing FdU (Sigma-Aldrich) at DIV6, and subsequently fed twice a week with serum-free media. Cells were maintained at 37°C with 5% CO₂.

At DIV16, neurons were transfected with 2 μg indicated plasmids per well (12-well plate) using Lipofectamine 2000 reagent (Invitrogen). Neurons were fixed at DIV18 with 4% PFA together with 4% sucrose in PBS buffer and mounted on slides for imaging. The Zeiss LSM 980 confocal microscope was used for imaging with multiple z-stacks. The quantification was done with ImageJ.

Golgi staining

FD Rapid GolgiStain Kit (PK401; FD NeuroTechnologies) was used to examine the histology of dendrites and dendritic spines in IQSEC2 F367A mutant mice and their WT littermates at 120 ± 5 days old of age. After mice were anesthetized with CO_2 and decapitated, the brain was rapidly removed and subjected to the procedures instructed by the kit manual. Sections with a thickness of $100~\mu m$ were cut on a vibrating microtome (VT1200S; Leica). The Zeiss LSM 980 confocal microscope was used for imaging CA1 dendrites with multiple z-stacks. The quantification was done with ImageJ.

Synapse electron microscopy

Hippocampal tissue from WT and F367A mice (n=5 per genotype) was fixed via transcardial perfusion with 2.5% glutaral-dehyde and 4% PFA in 0.1 M phosphate buffer (pH 7.4). After postfixation in 1% osmium tetroxide, samples were dehydrated in an ethanol series, embedded in Epon 812 resin, and polymerized at 60°C for 48 h. Ultrathin sections (70 nm) were cut using a Leica UC7 ultramicrotome, stained with uranyl acetate and lead citrate, and imaged on a Hitachi HT7800 transmission electron microscope at 80 kV. PSD length and thickness were quantified from \geq 50 asymmetric (type I) synapses per animal using ImageJ.

PSD preparation from the hippocampus

PSD fractionation was performed as previously described (Suzuki, 2011; Tian et al., 2021, *Preprint*), with modifications. Briefly, hippocampi were dissected and homogenized by passing the tissue through a 26-gauge needle 12 times in homogenization



buffer (320 mM sucrose, 10 mM HEPES, pH 7.4, 1 mM EDTA, and Roche protease inhibitor cocktail). The homogenate was centrifuged at 800 g for 10 min at 4°C to separate the P1 pellet and S1 supernatant. The S1 fraction was further centrifuged at 15,000 q for 20 min at 4°C to yield P2 and S2 fractions. The P2 pellet was resuspended in MilliQ water, adjusted to 4 mM HEPES, pH 7.4, and incubated with agitation at 4°C for 30 min. Following incubation, the resuspended P2 was centrifuged at 25,000 q for 20 min at 4°C to isolate synaptosomes (Syn) and the LS1 supernatant. The synaptosome fraction (Syn) was resuspended in 50 mM HEPES, pH 7.4, mixed with an equal volume of 1% Triton X-100, and incubated with agitation at 4°C for 15 min. The crude PSD fraction was then obtained by centrifugation at 32,000 q for 20 min at 4°C. To further purify the PSD, the pellet was resuspended and incubated a second time in 0.5% Triton X-100 at 4°C for 15 min, followed by centrifugation at 200,000 g for 1 h to yield the PSD pellet. In a parallel experiment, the crude PSD pellet was resuspended and incubated in ice-cold 3% sarcosyl for 10 min, followed by centrifugation at 200,000 q for 1 h to isolate the PSD_{core} pellet. All final pellets were resuspended in a loading buffer for subsequent western blot analysis. Western blotting was performed with the use of monoclonal antibody against IQSEC2 (made in-house), anti-PSD-95 (Mab1596; Sigma-Aldrich), anti-GluN2B (ab93610; Abcam), anti-GluA1 (Mab2263; Sigma-Aldrich), anti-GluA2 (Mab397; Sigma-Aldrich), and antiβ3-tubulin (5568S; Cell Signaling Technology).

Purification of recombinant proteins from Escherichia coli

Recombinant proteins were expressed in *E. coli* BL21 (DE3) cells (Agilent Technologies) in LB medium at 16°C for 16–20 h after IPTG induction. Protein purification was performed using Ni²⁺-NTA agarose affinity column (for His₆-tag proteins) followed by SEC with a column buffer containing 50 mM Tris, pH 8.2, 100–500 mM NaCl, 1 mM EDTA, and 1 mM DTT. His₆-/TRX-His₆-tags were cleaved by HRV-3C protease at 4°C overnight and removed by another step of SEC or ion-exchange chromatography. For measurements of protein-protein interactions or structure determination, purified proteins were assayed in a buffer containing 50 mM Tris, pH 8.2, 100 mM NaCl, and 1 mM DTT with the indicated concentration of EDTA or CaCl₂. For phase separation assays, purified proteins were finally exchanged into an assay buffer containing 25 mM HEPES, pH 7.4, 100 mM NaCl, and 1 mM TCEP.

ITC

ITC measurements were performed using a MicroCal VP-ITC calorimeter (Malvern). The experiment took place at 25°C in the assay buffer with 10–20 μM of each indicated protein in the sample cell titrated with its binder at 100–200 μM . Each titration point contained an injection of 10 μl aliquot delivered in 20 s with a 120-s interval between successive injections. Data were analyzed using the simple single-site–binding model by the Origin 7 software.

SEC coupled to multi-angle light scattering

SEC coupled to multi-angle light scattering (SEC-MALS) assay was performed on an AKTA purifier system (Cytiva) coupled with a static light scattering detector (miniDAWN, Wyatt) and a

differential refractive index detector (Optilab, Wyatt). Typically, 100 μ l of purified protein at an indicated concentration was loaded onto a Superose 12 10/300GL column in a column buffer composed of 50 mM Tris, pH 8.2, 100 mM NaCl, and 1 mM DTT, with 1 mM EDTA or 5 mM CaCl₂. Data were analyzed using ASTRA8 (Wyatt).

Fluorescent-based nucleotide exchange activity assays

GEF activity assay was performed as previously described (Bai et al., 2023). Briefly, nucleotide exchange kinetics were measured using bacterially purified $\Delta 17ARF1$ preloaded with GDP. Reactions were initiated by mixing ARF1-GDP with mantGTP and IQSEC2 proteins in an assay buffer (25 mM HEPES, pH 7.4, 100 mM NaCl, 1 mM MgCl₂, 1 mM DTT with 1 mM EGTA or 1 mM CaCl₂). FRET signals (excitation 297 nm/emission 450 nm) from ARF1-mantGTP formation were recorded every 10 s for 60 min at 30°C using a FlexStation 3 plate reader (Molecular Devices). $k_{\rm obs}$ values were derived from one-phase exponential fits, and catalytic efficiency ($k_{\rm cat}/K_{\rm M}$) was calculated via linear regression of $k_{\rm obs}$ versus [GEF] (Michaelis–Menten kinetics). All measurements were repeated four times. Data were analyzed using GraphPad Prism.

Crystallization and structure determination

Crystals of IQSEC2 CC domain were obtained by the hanging drop vapor-diffusion method at 16°C. CC (aa 12–74) protein was purified and concentrated to a concentration of 4 mg/ml in a buffer containing 25 mM Tris, pH 8.2, 100 mM NaCl, and 1 mM DTT. The complex solution was mixed with equal volume (1 $\mu l+1~\mu l)$ of the reservoir buffer containing 0.1 M sodium malonate, pH 5.0, and 12% wt/vol polyethylene glycol 3,350 for crystallization. Crystals were cryoprotected with 30% (vol/vol) glycerol and flash-cooled to 100 K.

X-ray diffraction data were collected at the BL19U1 beamlines at the Shanghai Synchrotron Radiation Facility. Diffraction data were processed using HKL2000 (Otwinowski and Minor, 1997). The initial model was found using the *ab initio* phasing program ARCIMBOLDO (Rodriguez et al., 2009). Manual model building and refinement were carried out iteratively using Coot (Emsley et al., 2010) and PHENIX (Adams et al., 2010). The final models were validated by MolProbity (Chen et al., 2010), and statistics were summarized in Table 1. All structure figures were drawn using PyMOL (http://www.pymol.org).

Lipid-protein interaction assay

Membrane lipid-binding analysis of His $_6$ -tagged Sec7-PH was conducted using membrane lipid Strips (P-6002; Echelon Bioscience) or PIP Strips (P-6001; Echelon Bioscience). Membranes were blocked by TBST with 3% BSA for 1 h at room temperature, followed by incubation with 2 μ g/ml His-Sec7-PH for 1 h in blocking buffer. After washing three times with TBST, the membrane was blotted with anti-His antibody (H1029; Sigma-Aldrich).

Liposome preparation and co-sedimentation assay

Brain lipid extracts (Folch fraction I, B1502; Sigma-Aldrich) or mixed lipids as indicated were resuspended to bring the final lipid concentration to 2.5 mg/ml in a buffer containing 25 mM



HEPES, pH 7.4, 100 mM NaCl, and 1 mM TCEP, then sonicated, and extruded through a 0.22- μ m filter. The protein sample was incubated with liposomes in a 100 μ l final volume for 30 min at room temperature and then spun at 55,000 rpm for 30 min at 20°C in a Beckman MLA-130 rotor. Right after centrifugation, the supernatant and pellet were separated. The pellet was brought to the same volume as the supernatant. Proteins recovered in supernatant and pellet were analyzed by SDS-PAGE with Coomassie blue staining.

Sedimentation and imaging assays of in vitro phase separation

The concentrations of proteins in all assays were determined by NanoDrop 2000 spectrophotometer (Thermo Fisher Scientific) and precleared by high-speed centrifuging at 25°C before each phase separation assay.

For sedimentation assays, proteins were mixed at designated combinations and conditions in the buffer containing 25 mM HEPES, pH 7.4, 100 mM NaCl, and 1 mM TCEP. After 10-min incubation at room temperature, the mixtures were centrifuged at 16,873 g for 10 min at 25°C. Right after centrifugation, the supernatant and pellet were separated. The pellet was brought to the same volume as the supernatant. Proteins recovered in supernatant and pellet were analyzed by SDS-PAGE with Coomassie Blue staining. The band intensities in SDS-PAGE gels were quantified by ImageJ software. Relative and absolute amounts of proteins in the supernatant and pellet were calculated based on the input amounts and relative band intensities. Data from three repeats were presented as mean \pm SD.

DIC and fluorescence imaging assays were performed on a Zeiss LSM 980 confocal microscope. Proteins were sparsely labeled with Alexa Fluor 488 NHS ester (Thermo Fisher Scientific) and Cy3 NHS ester (AAT Bioquest) at the final labeling ratio of 2%.

Quantification and statistical analysis

Detailed statistical parameters, including definitions and exact values (e.g., number of experiments, number of cells, etc.), as well as distributions and deviations, were provided in the figures and their corresponding legends. For comparisons between groups, unpaired or paired two-tailed Student's t tests were employed when the assumptions of normality (assessed using the Shapiro–Wilk test) and equal variance (verified via the F test) were satisfied. For comparisons involving more than two groups, one-way ANOVA followed by Tukey's post hoc multiple comparison test was used. Statistical significance was defined as P < 0.05. All statistical analyses were conducted using GraphPad Prism software (version 9.0, GraphPad Software).

Online supplemental material

Fig. S1 shows the behavioral phenotyping of IQSEC2 F367A mice. Fig. S2 shows the biochemical and biophysical characterization of IQSEC2 membrane interaction and oligomerization. Fig. S3 shows FRAP analysis of IQSEC2 puncta in HeLa cells. Fig. S4 shows the Ca²⁺-induced phase separation of IQSEC2. Fig. S5 shows that IQSEC2 phase separation promotes PSD-95 integration into the PSD condensates. Video 1 shows the puncta fusion process in response to calcium influx in HeLa cells expressing mCherry-IQSEC2.

Data availability

The atomic coordinates of IQSEC2 CC domain can be accessed at the Protein Data Bank with the accession number of 9M46.

Acknowledgments

We thank the BL19U1 beamlines at the National Facility for Protein Science Shanghai for X-ray beam time.

This work was supported by grants from the Shenzhen Medical Research Fund (B2302039) to Mingjie Zhang and National Natural Science Foundation of China (32494762 and 32200773 to Guanhua Bai, 32200795 to Hao Li, and 31721002 and 81920208014 to Youming Lu). Chinese National Programs for Brain Science and Brain-like Intelligence Technology (2025ZD0217900 and 2022ZD0205800 to Guanhua Bai) and Natural Science Foundation of Hubei Province (2022CFB608 to Hao Li). Shenzhen Talent Program (KQTD20210811090115021), Shenzhen Science and Technology Basic Research Program (JCYJ20220818100215033), Guangdong Innovative and Entrepreneurial Research Team Program (2021ZT09Y104), and Key-Area Research and Development Program of Guangdong Province (2023B0303010001) to Mingjie Zhang.

Author contributions: Guanhua Bai: conceptualization, data curation, formal analysis, funding acquisition, investigation, methodology, project administration, resources, supervision, validation, visualization, and writing—original draft, review, and editing. Ruifeng Huang: data curation, formal analysis, investigation, project administration, resources, validation, visualization, and writing—original draft, review, and editing. Xinyue Nan: data curation, formal analysis, investigation, methodology, validation, and visualization. Mengru Zhuang: methodology. Meiling Wu: data curation, formal analysis, methodology, project administration, and resources. Yinmiao Lian: data curation, formal analysis, investigation, and resources. Visualization, Qixu Cai: investigation. Honglei Tian: methodology and resources. Youming Lu: conceptualization, funding acquisition, resources, and supervision. Hao Li: conceptualization, data curation, formal analysis, funding acquisition, investigation, methodology, project administration, resources, supervision, validation, visualization, and writing-original draft, review, and editing. Mingjie Zhang: conceptualization, funding acquisition, project administration, resources, supervision, and writing—original draft, review, and editing.

Disclosures: The authors declare no competing interests exist.

Submitted: 18 March 2025 Revised: 12 August 2025 Accepted: 15 September 2025

References

Adams, P.D., P.V. Afonine, G. Bunkóczi, V.B. Chen, I.W. Davis, N. Echols, J.J. Headd, L.-W. Hung, G.J. Kapral, R.W. Grosse-Kunstleve, et al. 2010. PHENIX: A comprehensive Python-based system for macromolecular structure solution. Acta Crystallogr. D Biol. Crystallogr. 66:213–221. https://doi.org/10.1107/S0907444909052925

Aizel, K., V. Biou, J. Navaza, L.V. Duarte, V. Campanacci, J. Cherfils, and M. Zeghouf. 2013. Integrated conformational and lipid-sensing regulation



- of endosomal ArfGEF BRAG2. Plos Biol. 11:e1001652. https://doi.org/10.1371/journal.pbio.1001652
- Araki, Y., K.E. Rajkovich, E.E. Gerber, T.R. Gamache, R.C. Johnson, T.H.N. Tran, B. Liu, Q. Zhu, I. Hong, A. Kirkwood, and R. Huganir. 2024. SynGAP regulates synaptic plasticity and cognition independently of its catalytic activity. *Science*. 383:eadkl291. https://doi.org/10.1126/science.adkl291
- Araki, Y., M. Zeng, M. Zhang, and R.L. Huganir. 2015. Rapid dispersion of SynGAP from synaptic spines triggers AMPA receptor insertion and spine enlargement during LTP. Neuron. 85:173–189. https://doi.org/10 .1016/j.neuron.2014.12.023
- Bai, G., H. Li, P. Qin, Y. Guo, W. Yang, Y. Lian, F. Ye, J. Chen, M. Wu, R. Huang, et al. 2023. Ca²⁺-induced release of IQSEC2/BRAG1 autoinhibition under physiological and pathological conditions. J. Cell Biol. 222:e202307117. https://doi.org/10.1083/jcb.202307117
- Brown, J.C., A. Petersen, L. Zhong, M.L. Himelright, J.A. Murphy, R.S. Walikonis, and N.Z. Gerges. 2016. Bidirectional regulation of synaptic transmission by BRAG1/IQSEC2 and its requirement in long-term depression. *Nat. Commun.* 7:11080. https://doi.org/10.1038/ncomms11080
- Chen, V.B., W.B. Arendall 3rd, J.J. Headd, D.A. Keedy, R.M. Immormino, G.J. Kapral, L.W. Murray, J.S. Richardson, and D.C. Richardson. 2010. MolProbity: All-atom structure validation for macromolecular crystallography. Acta Crystallogr. D Biol. Crystallogr. 66:12–21. https://doi.org/10.1107/S0907444909042073
- Chen, X., Q. Cai, J. Zhou, S.J. Pleasure, H. Schulman, M. Zhang, and R.A. Nicoll. 2024. CaMKII autophosphorylation is the only enzymatic event required for synaptic memory. *Proc. Natl. Acad. Sci. USA*. 121: e2402783121. https://doi.org/10.1073/pnas.2402783121
- Clargo, A.M., A.R. Hudson, W. Ndlovu, R.J. Wootton, L.A. Cremin, V.L. O'Dowd, C.R. Nowosad, D.O. Starkie, S.P. Shaw, J.E. Compson, et al. 2014. The rapid generation of recombinant functional monoclonal antibodies from individual, antigen-specific bone marrow-derived plasma cells isolated using a novel fluorescence-based method. MAbs. 6:143–159. https://doi.org/10.4161/mabs.27044
- Dosemeci, A., A.J. Makusky, E. Jankowska-Stephens, X. Yang, D.J. Slotta, and S.P. Markey. 2007. Composition of the synaptic PSD-95 complex. *Mol. Cell. Proteomics*. 6:1749–1760. https://doi.org/10.1074/mcp.M700040-MCP200
- Emsley, P., B. Lohkamp, W.G. Scott, and K. Cowtan. 2010. Features and development of coot. *Acta Crystallogr. D Biol. Crystallogr.* 66:486-501. https://doi.org/10.1107/S0907444910007493
- Halt, A.R., R.F. Dallapiazza, Y. Zhou, I.S. Stein, H. Qian, S. Juntti, S. Wojcik, N. Brose, A.J. Silva, and J.W. Hell. 2012. CaMKII binding to GluN2B is critical during memory consolidation. Embo J. 31:1203–1216. https://doi.org/10.1038/emboj.2011.482
- Hinze, S.J., M.R. Jackson, S. Lie, L. Jolly, M. Field, S.C. Barry, R.J. Harvey, and C. Shoubridge. 2017. Incorrect dosage of IQSEC2, a known intellectual disability and epilepsy gene, disrupts dendritic spine morphogenesis. *Transl. Psychiatry*. 7:e1110. https://doi.org/10.1038/tp.2017.81
- Incontro, S., J. Díaz-Alonso, J. Iafrati, M. Vieira, C.S. Asensio, V.S. Sohal, K.W. Roche, K.J. Bender, and R.A. Nicoll. 2018. The CaMKII/NMDA receptor complex controls hippocampal synaptic transmission by kinase-dependent and independent mechanisms. *Nat. Commun.* 9:2069. https://doi.org/10.1038/s41467-018-04439-7
- Jia, B., Z. Shen, S. Zhu, J. Huang, Z. Liao, S. Zhao, H. Li, S. Chen, Y. Xu, Y. Wang, et al. 2025. Shank3 oligomerization governs material properties of the postsynaptic density condensate and synaptic plasticity. Cell. S0092-8674(25)00913-4. https://doi.org/10.1016/j.cell.2025.07.047
- Jian, X., J.M. Gruschus, E. Sztul, and P.A. Randazzo. 2012. The pleckstrin homology (PH) domain of the Arf exchange factor Brag2 is an allosteric binding site. J. Biol. Chem. 287:24273–24283. https://doi.org/10.1074/jbc .M112.368084
- Karandur, D., A. Nawrotek, J. Kuriyan, and J. Cherfils. 2017. Multiple interactions between an Arf/GEF complex and charged lipids determine activation kinetics on the membrane. Proc. Natl. Acad. Sci. USA. 114: 11416–11421. https://doi.org/10.1073/pnas.1707970114
- Li, X., H. Yu, B. Zhang, L. Li, W. Chen, Q. Yu, X. Huang, X. Ke, Y. Wang, W. Jing, et al. 2022. Molecularly defined and functionally distinct cholinergic subnetworks. *Neuron*. 110:3774–3788.e7. https://doi.org/10.1016/j.neuron.2022.08.025
- Lopergolo, D., F. Privitera, G. Castello, C. Lo Rizzo, M.A. Mencarelli, A.M. Pinto, F. Ariani, A. Currò, V. Lamacchia, R. Canitano, et al. 2021. IQSEC2 disorder: A new disease entity or a Rett spectrum continuum? Clin. Genet. 99:462-474. https://doi.org/10.1111/cge.13908

- Lowenthal, M.S., S.P. Markey, and A. Dosemeci. 2015. Quantitative mass spectrometry measurements reveal stoichiometry of principal post-synaptic density proteins. *J. Proteome Res.* 14:2528–2538. https://doi.org/10.1021/acs.jproteome.5b00109
- Mehta, A., Y. Shirai, É. Kouyama-Suzuki, M. Zhou, T. Yoshizawa, T. Yanagawa, T. Mori, and K. Tabuchi. 2021. IQSEC2 deficiency results in abnormal social behaviors relevant to autism by affecting functions of neural circuits in the medial prefrontal cortex. Cells. 10:2724. https://doi.org/10.3390/cells10102724
- Meyer, L., T. López, R. Espinosa, C.F. Arias, C. Vollmers, and R.M. DuBois. 2019. A simplified workflow for monoclonal antibody sequencing. Plos One. 14:e0218717. https://doi.org/10.1371/journal.pone.0218717
- Mignot, C., A.C. McMahon, C. Bar, P.M. Campeau, C. Davidson, J. Buratti, C. Nava, M.-L. Jacquemont, M. Tallot, M. Milh, et al. 2019. IQSEC2-related encephalopathy in males and females: A comparative study including 37 novel patients. *Genet. Med.* 21:837–849. https://doi.org/10.1038/s41436-018-0268-1
- Murphy, J.A., O.N. Jensen, and R.S. Walikonis. 2006. BRAG1, a Sec7 domain-containing protein, is a component of the postsynaptic density of excitatory synapses. *Brain Res.* 1120:35-45. https://doi.org/10.1016/j.brainres.2006.08.096
- Myers, K.R., G. Wang, Y. Sheng, K.K. Conger, J.E. Casanova, and J.J. Zhu. 2012. Arf6-GEF BRAG1 regulates JNK-mediated synaptic removal of GluA1containing AMPA receptors: A new mechanism for nonsyndromic X-linked mental disorder. J. Neurosci. 32:11716–11726. https://doi.org/10 .1523/JNEUROSCI.1942-12.2012
- Otwinowski, Z., and W. Minor. 1997. Processing of X-ray diffraction data collected in oscillation mode. *Methods Enzymol.* 276:307–326. https://doi.org/10.1016/S0076-6879(97)76066-X
- Petersen, A., J.C. Brown, and N.Z. Gerges. 2020. BRAG1/IQSEC2 as a regulator of small GTPase-dependent trafficking. Small GTPases. 11:1–7. https://doi.org/10.1080/21541248.2017.1361898
- Radley, J.A., R.B.G. O'Sullivan, S.E. Turton, H. Cox, J. Vogt, J. Morton, E. Jones, S. Smithson, K. Lachlan, J. Rankin, et al. 2019. Deep phenotyping of 14 new patients with IQSEC2 variants, including monozygotic twins of discordant phenotype. Clin. Genet. 95:496–506. https://doi.org/10.1111/cge.13507
- Rodriguez, D.D., C. Grosse, S. Himmel, C. González, I.M. de Ilarduya, S. Becker, G.M. Sheldrick, and I. Usón. 2009. Crystallographic ab initio protein structure solution below atomic resolution. *Nat. Methods.* 6: 651–653. https://doi.org/10.1038/nmeth.1365
- Rogers, E.J., R. Jada, K. Schragenheim-Rozales, M. Sah, M. Cortes, M. Florence, N.S. Levy, R. Moss, R.S. Walikonis, R. Palty, et al. 2019. An IQSEC2 mutation associated with intellectual disability and autism results in decreased surface AMPA receptors. Front. Mol. Neurosci. 12:43. https://doi.org/10.3389/fnmol.2019.00043
- Sah, M., A.N. Shore, S. Petri, A. Kanber, M. Yang, M.C. Weston, and W.N. Frankel. 2020. Altered excitatory transmission onto hippocampal interneurons in the IQSEC2 mouse model of X-linked neuro-developmental disease. Neurobiol. Dis. 137:104758. https://doi.org/10.1016/j.nbd.2020.104758
- Sajan, S.A., S.N. Jhangiani, D.M. Muzny, R.A. Gibbs, J.R. Lupski, D.G. Glaze, W.E. Kaufmann, S.A. Skinner, F. Annese, M.J. Friez, et al. 2017. Enrichment of mutations in chromatin regulators in people with Rett syndrome lacking mutations in MECP2. Genet. Med. 19:13–19. https://doi .org/10.1038/gim.2016.42
- Sakagami, H., M. Sanda, M. Fukaya, T. Miyazaki, J. Sukegawa, T. Yanagisawa, T. Suzuki, K. Fukunaga, M. Watanabe, and H. Kondo. 2008. IQ-ArfGEF/BRAG1 is a guanine nucleotide exchange factor for Arf6 that interacts with PSD-95 at postsynaptic density of excitatory synapses. Neurosci. Res. 60:199-212. https://doi.org/10.1016/j.neures.2007.10.013
- Sanda, M., A. Kamata, O. Katsumata, K. Fukunaga, M. Watanabe, H. Kondo, and H. Sakagami. 2009. The postsynaptic density protein, IQ-ArfGEF/BRAG1, can interact with IRSp53 through its proline-rich sequence. Brain Res. 1251:7-15. https://doi.org/10.1016/j.brainres.2008.11.061
- Scholz, R., S. Berberich, L. Rathgeber, A. Kolleker, G. Kohr, and H.C. Kornau. 2010. AMPA receptor signaling through BRAG2 and Arf6 critical for long-term synaptic depression. *Neuron*. 66:768–780. https://doi.org/10 .1016/j.neuron.2010.05.003
- Shoubridge, C., R.J. Harvey, and T. Dudding-Byth. 2019. IQSEC2 mutation update and review of the female-specific phenotype spectrum including intellectual disability and epilepsy. Hum. Mutat. 40:5–24. https://doi.org/10.1002/humu.23670

i et al. Journal of Cell Biology 18 of 19



- Suzuki, T. 2011. In Isolation of Synapse Subdomains by Subcellular Fractionation Using Sucrose Density Gradient Centrifugation. Vol. 57. K. Li, editor. Humana Press, Totowa, NJ. 47-61.
- Tian, M., Q. Chen, A.R. Graves, H.L. Goldschmidt, R.C. Johnson, D.R. Weinberger, and R.L. Huganir. 2021. KIBRA-PKCγ signaling pathway modulates memory performance in mice and humans. bioRxiv. https://doi.org/10.1101/2021.10.26.465926 (Preprint posted October 28, 2021).
- Tullis, J.E., M.E. Larsen, N.L. Rumian, R.K. Freund, E.E. Boxer, C.N. Brown, S.J. Coultrap, H. Schulman, J. Aoto, M.L. Dell'Acqua, and K.U. Bayer. 2023. LTP induction by structural rather than enzymatic functions of CaMKII. *Nature*. 621:146–153. https://doi.org/10.1038/s41586-023-06465-y
- Wu, X., Z. Shen, and M. Zhang. 2025. Phase separation-mediated compartmentalization underlies synapse formation and plasticity. Annu. Rev. Neurosci. 48:149-168. https://doi.org/10.1146/annurev-neuro-112723 -040159
- Yang, H., L. Shi, B.-A. Wang, D. Liang, C. Zhong, W. Liu, Y. Nie, J. Liu, J. Zhao, X. Gao, et al. 2012. Generation of genetically modified mice by oocyte injection of androgenetic haploid embryonic stem cells. *Cell*. 149: 605–617. https://doi.org/10.1016/j.cell.2012.04.002

- Zakeri, B., J.O. Fierer, E. Celik, E.C. Chittock, U. Schwarz-Linek, V.T. Moy, and M. Howarth. 2012. Peptide tag forming a rapid covalent bond to a protein, through engineering a bacterial adhesin. Proc. Natl. Acad. Sci. USA. 109:E690-E697. https://doi.org/10.1073/pnas.1115485109
- Zeng, M., X. Chen, D. Guan, J. Xu, H. Wu, P. Tong, and M. Zhang. 2018. Reconstituted postsynaptic density as a molecular platform for understanding synapse formation and plasticity. *Cell*. 174:1172–1187.e16. https://doi.org/10.1016/j.cell.2018.06.047
- Zeng, M., Y. Shang, Y. Araki, T. Guo, R.L. Huganir, and M. Zhang. 2016. Phase transition in postsynaptic densities underlies formation of synaptic complexes and synaptic plasticity. *Cell.* 166:1163–1175.e12. https://doi. org/10.1016/j.cell.2016.07.008
- Zhang, Y., W. Kong, Y. Gao, X. Liu, K. Gao, H. Xie, Y. Wu, Y. Zhang, J. Wang, F. Gao, et al. 2015. Gene mutation analysis in 253 Chinese children with unexplained epilepsy and intellectual/developmental disabilities. Plos One. 10:e0141782. https://doi.org/10.1371/journal.pone.0141782
- Zhong, C., Q. Yin, Z. Xie, M. Bai, R. Dong, W. Tang, Y.-H. Xing, H. Zhang, S. Yang, L.-L. Chen, et al. 2015. CRISPR-Cas9-mediated genetic screening in mice with haploid embryonic stem cells carrying a guide RNA library. Cell Stem Cell. 17:221–232. https://doi.org/10.1016/j.stem.2015.06.005



Supplemental material



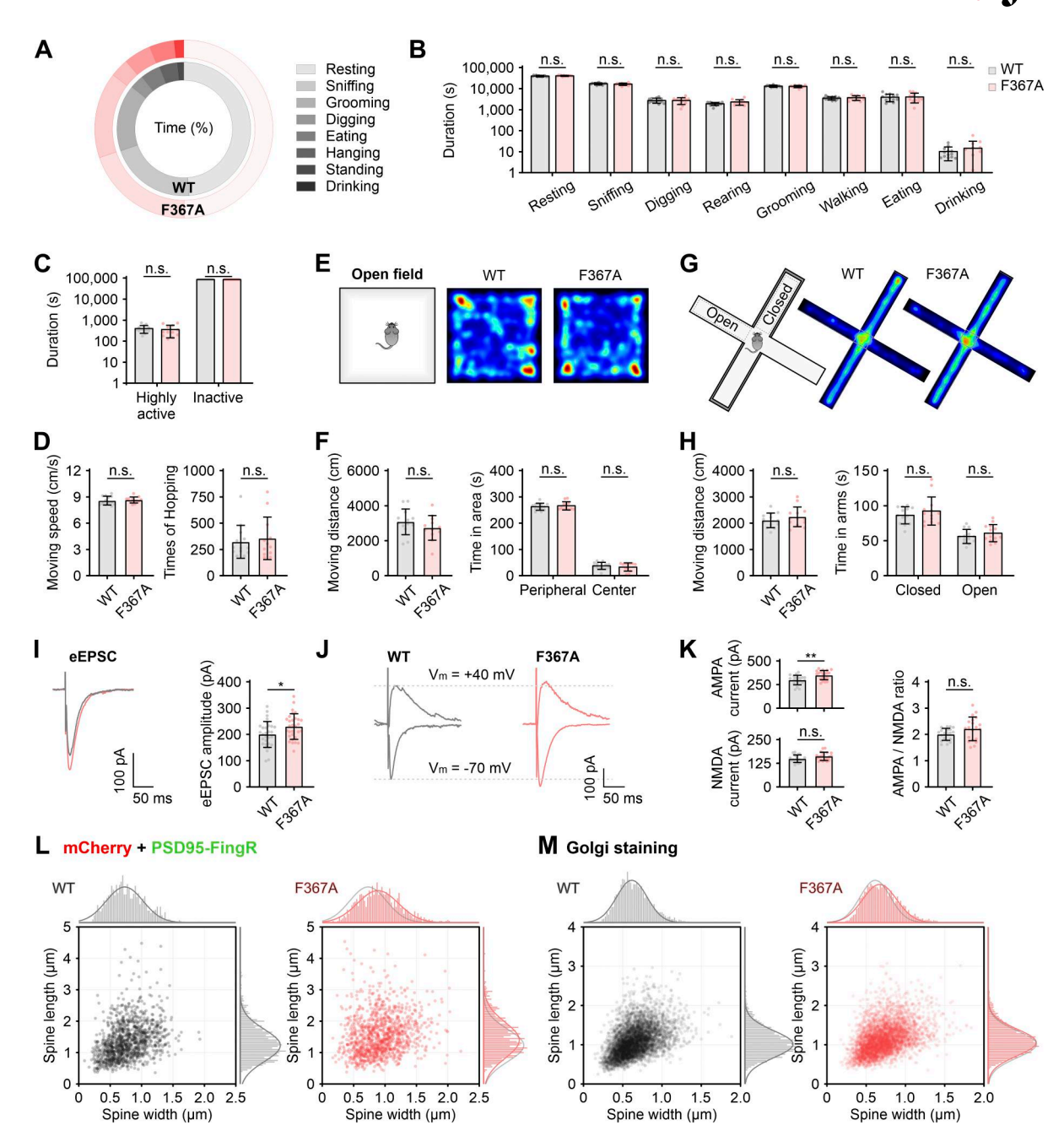


Figure S1. Behavioral phenotyping of IQSEC2 F367A mice. (A) Pie chart summary showing 24-h natural spontaneous behavior recordings of F367A mutant mice and their WT littermates. (B) Bar graphs showing the duration of examined spontaneous behaviors in the 24-h recordings. Data are presented as mean ± SD (WT: 13 mice; F367A: 12 mice; n.s., not significant; unpaired t test). (c) Bar graphs showing the duration of activity state in the 24-h recordings. Data are presented as mean ± SD (WT: 13 mice; F367A: 12 mice; n.s., not significant; unpaired t test). (D) Bar graphs showing the moving speed and frequency of hopping in the 24-h recording. Data are presented as mean ± SD (WT: 13 mice; F367A: 12 mice; n.s., not significant; unpaired t test). (E) Representative exploration heatmaps of F367A mutant mice and their WT littermates in the open-field test. (F) Quantification of open-field parameters, including total moving distance (cm) and time spent (s) in the peripheral and central areas. Data are presented as mean ± SD (WT: 13 mice; F367A: 12 mice; n.s., not significant; unpaired t test). (G) Scheme of the elevated plus maze and representative exploration heatmaps of F367A mutant mice and their WT littermates. (H) Quantification of the elevated plus maze parameters, including total moving distance (cm) and time spent (s) in the closed and open arms. Data are presented as mean ± SD (WT/ F367A: 13 mice; n.s., not significant; unpaired t test). (I) Representative traces of initial eEPSCs and comparison of average eEPSC amplitudes recorded from CA1 pyramidal neurons in the brain slice of IQSEC2 WT (gray) and F367A mutant mice (red). Individual average values per neuron are indicated as dots. Data are presented as mean ± SD (30 neurons from 3 mice per group; *P < 0.05; unpaired t test). (1) The eEPSCs were recorded in CA1 pyramidal neurons in the presence of 20 µM bicuculline. The AMPAR-mediated EPSCs were recorded at -70 mV, while NMDAR-mediated EPSCs were recorded at +40 mV in the presence of both 20 μM bicuculline and 20 μM CNQX. (K) The amplitude of AMPAR EPSCs, NMDAR EPSCs, and their ratio in individual neurons. Data are presented as mean ± SD (20 neurons from 3 mice per group; n.s., not significant; **P < 0.01; unpaired t test). (L) Two-dimensional plots and frequency distribution histograms of spine length and spine head width in cultured hippocampus neurons from F367A mutant mice and their WT littermates as in Fig. 3, A and B. (M) Two-dimensional plots and frequency distribution histograms of spine length and spine head width in Golgi-stained pyramidal neurons in the hippocampus CA1 region from F367A mutant mice and their WT littermates, as in Fig. 3, C and D. CNQX, 6-cyano-7-nitroquinoxaline-2,3-dione.



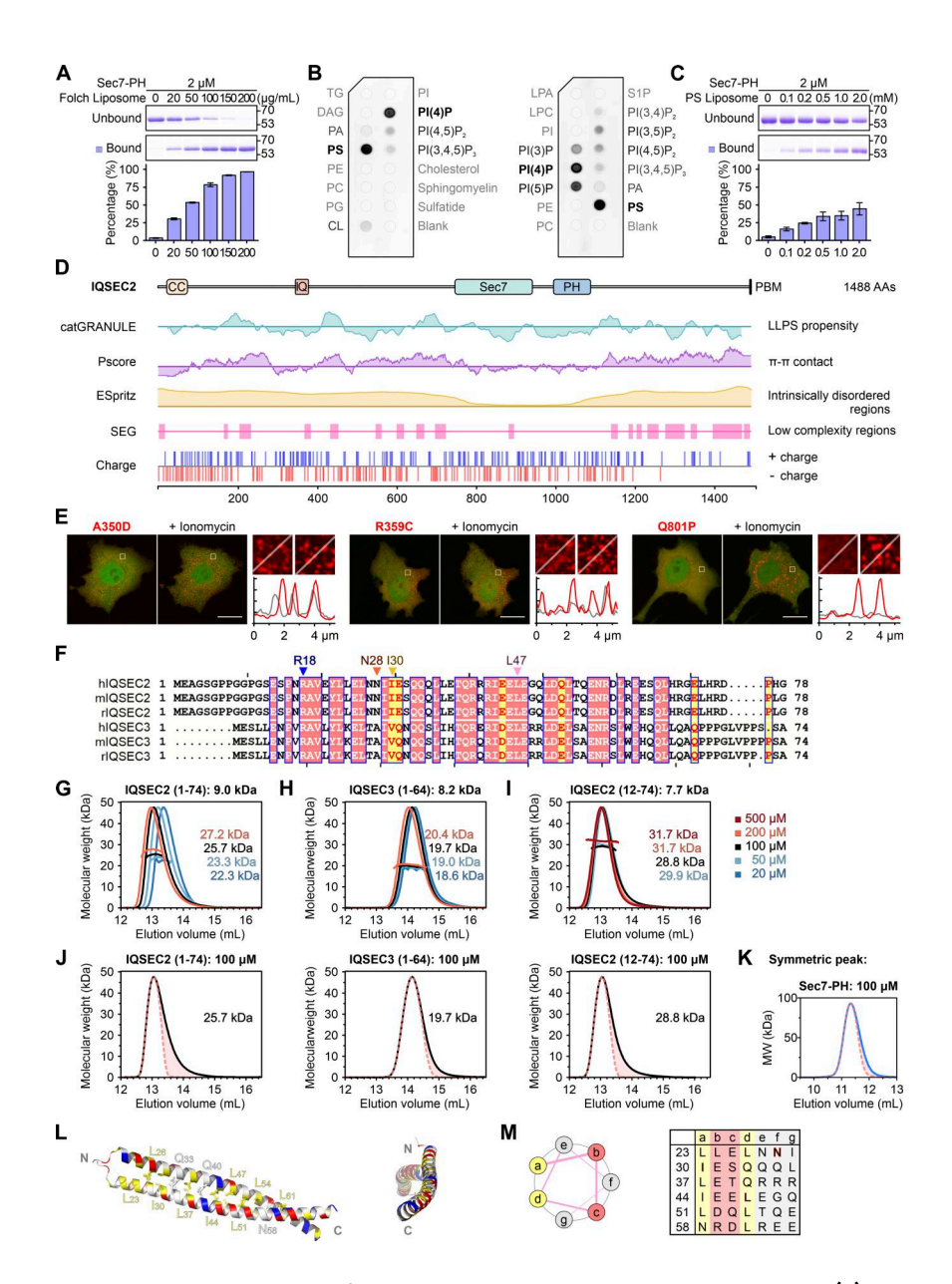


Figure S2. Biochemical and biophysical characterization of IQSEC2 membrane interaction and oligomerization. (A) Co-sedimentation assay showing that the Sec7-PH tandem of IOSEC2 interacts with liposomes prepared from the Folch fraction of lipids. Data from three repeated experiments were presented as mean ± SD. (B) Protein-lipid overlay assay of His-Sec7-PH protein with membrane lipids. TG, triglyceride; DAG, diacylglycerol; PA, phosphatidic acid; PS, phosphatidylserine; PE, phosphatidylethanolamine; PC, phosphatidylcholine; PG, phosphatidylglycerol; CL, cardiolipin; PI, phosphatidylinositol; PI(3)P, phosphatidylinositol 3-phosphate; PI(4)P, phosphatidylinositol 4-phosphate; PI(5)P, phosphatidylinositol 5-phosphate; PI(3,4)P₂, phosphatidylinositol 3,4phosphate; PI(3,5)P₂, phosphatidylinositol 3,5-phosphate; PI(4,5)P₂, phosphatidylinositol 4,5-phosphate; PI(3,4,5)P₃, phosphatidylinositol 3,4,5-phosphate; LPA, lysophosphatidic acid; LPC, lysophosphatidylcholine; S1P, sphingosine-1-phosphate. (C) Co-sedimentation assay showing the Sec7-PH tandem of IQSEC2 interacts with PS liposomes (48% POPC and 52% DOPS). Data from three repeated experiments were presented as mean ± SD. (D) Sequence analysis by PhaSePred showing the loop regions connecting the functional domains of IQSEC2 contain several stretches of intrinsically disordered sequences prone to phase separation. (E) Representative images of HeLa cells expressing mutants of mCherry-IQSEC2 before and after ionomycin treatment. Line-scanning plots showing the relative mCherry fluorescent signal distribution before and after ionomycin stimulation in the zoomed-in images. Scale bar, 20 µm. (F) Sequence alignment analysis of IQSECs' N-terminal CC domain. The mutated residues in Fig. 5 are denoted. (G) SEC-MALS analysis of IQSEC2 CC (1-74) domain at concentrations from 200 to 20 μM (as shown), indicating a concentration-dependent dissociation of tetramers. (H) SEC-MALS analysis of IQSEC3 CC (1–64) domain at concentrations from 200 to 20 μM (as shown) suggests its concentration-dependent oligomerization. (I) SEC-MALS analysis of IQSEC2 CC (12–74) domain at concentrations from 500 to 50 µM (as shown) suggests it forms a stable tetramer. Deletion of the disordered region preceding the conserved sequences of IQSEC2 appears to slightly enhance the propensity of its CC domain to form tetrameric structures. (J) SEC-MALS traces of IQSEC CC at 100 μM (solid lines) with their corresponding symmetrized fits (dashed lines). The obvious tailing of the elution profiles relative to the ideal fits suggests either conformational heterogeneity or dynamic oligomerization. (K) Representative SEC-MALS trace of the well-folded Sec7-PH tandem domain (solid line) overlaid with a symmetrized fit of the peak (dashed line) demonstrating ideal monodisperse behavior. (L) Cartoon representation showing the dimerization interface of the CC dimer unit. The side chains of the residues involved in the dimer interface are drawn in the stick model. (M) Helical wheel diagram illustrating the heptad repeats and hydrophobic core residues in the CC domain. Residues at "a" and "d" positions forming the hydrophobic core of the CC are highlighted in yellow. Source data are available for this figure: SourceData FS2.

Bai et al. Journal of Cell Biology



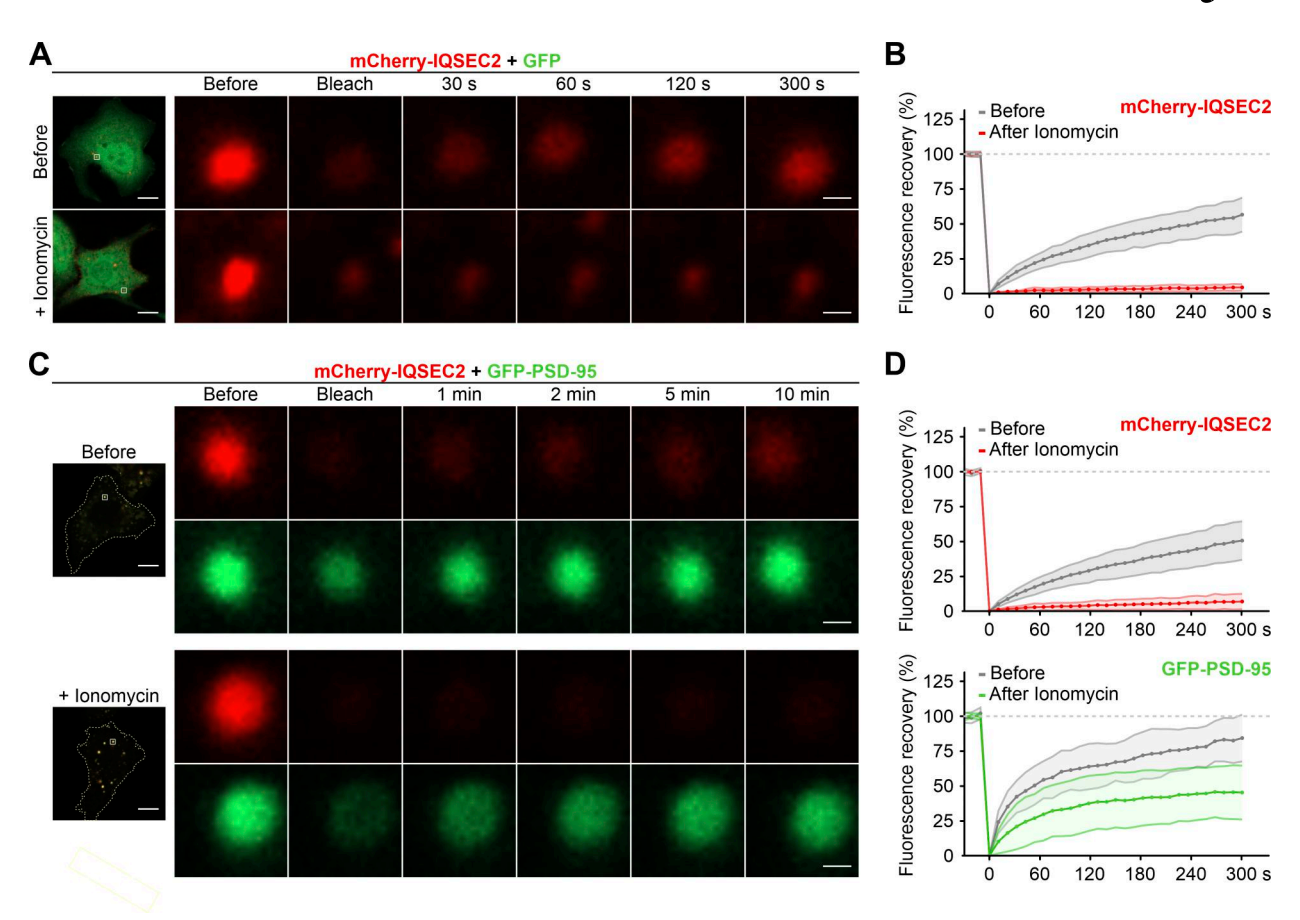


Figure S3. **FRAP analysis of IQSEC2 puncta in HeLa cells. (A and B)** HeLa cells were co-transfected with mCherry-IQSEC2 and GFP and imaged after 6–8 h of expression. FRAP was performed under untreated conditions (to assess baseline IQSEC2 puncta recovery) and after 5-min ionomycin treatment followed by medium wash (to evaluate calcium-dependent mobility changes). For quantitative analysis, the average intensity of frames before photobleaching was normalized to 100%, and the intensity right after the bleaching was set to 0%. The FRAP curves represent averaged results from 42 bleached regions with a bleaching beam diameter of 2 μ m (18 cells from four batches of cultures). Scale bar, 10 μ m. Scale bar for the zoomed-in images is 0.5 μ m. Data were presented as mean \pm SD. (**C and D**) HeLa cells were co-transfected with mCherry-IQSEC2 and GFP-PSD-95. FRAP conditions and normalization are the same as in A and B. The FRAP curves represent averaged results from 30 bleached regions with a bleaching beam diameter of 2 μ m (12 cells from four batches of cultures). Scale bar, 10 μ m. Scale bar for the zoomed-in images is 0.5 μ m. Data were presented as mean \pm SD.



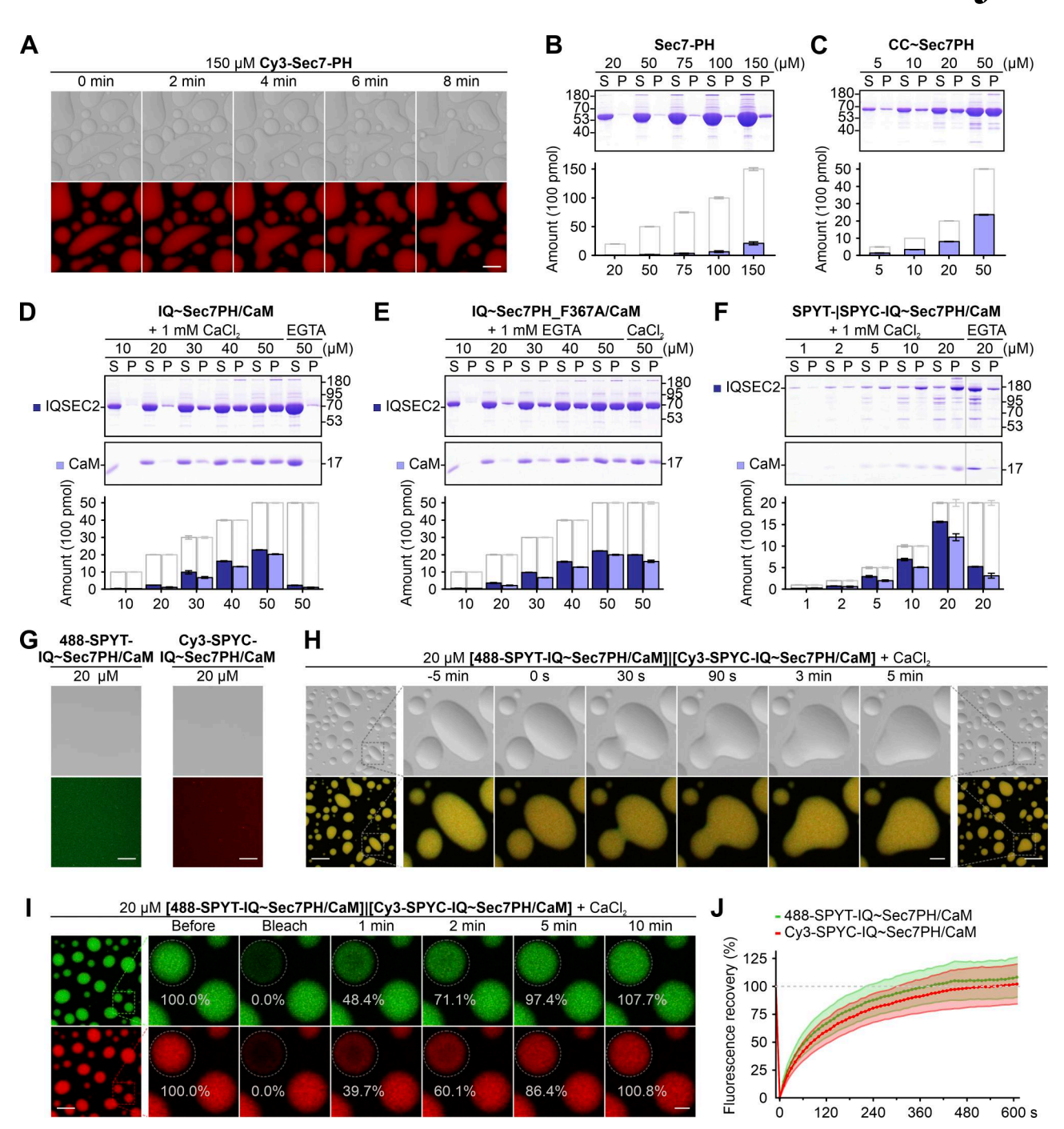


Figure S4. Ca²+-induced phase separation of IQSEC2. (A) Time-lapse imaging showing the fusion of Sec7-PH droplets into larger ones. Scale bar, 10 μm. (B) Representative SDS-PAGE of sedimentation experiments (upper panel) and quantification of protein amounts in the supernatant (S, gray columns) and pellet (P, blue columns) (lower panel) showing that Sec7-PH protein alone undergoes phase separation at high concentrations. Data from three repeated experiments were presented as mean ± SD. (C) Sedimentation experiments showing that CC~Sec7PH protein undergoes phase separation at lower concentrations compared with Sec7-PH. Data from three repeated experiments were presented as mean ± SD. (D and E) Sedimentation experiments showing the Ca²+-induced phase separation of IQ~Sec7PH/CaM and the Ca²+-independent phase separation of IQ~Sec7PH_F367A/CaM. Data from three repeated experiments were presented as mean ± SD. (F) Sedimentation experiments showing the Ca²+-induced phase separation of SPYT|SPYC-IQ~Sec7PH/CaM. Data from three repeated experiments were presented as mean ± SD. (G) Fluorescence images show that the SPYT-IQ~Sec7PH/CaM and SPYC-IQ~Sec7PH/CaM alone form homogeneous dilute solutions at the 20 μM concentration. Scale bar, 10 μm. (H) Time-lapse imaging showing the fusion of SPYT|SPYC-IQ~Sec7PH/CaM droplets into a larger one. Scale bar, 10 μm. Scale bar for the zoomed-in images, 2 μm. (I and J) FRAP analysis showing the dynamic component exchanges between the droplet and dilute solution. Scale bar, 10 μm. Scale bar for the zoomed-in images, 2 μm. The FRAP curves represent averaged results from 30 bleached regions with a diameter of 4.5 μm. Data were presented as mean ± SD. Source data are available for this figure: SourceData FS4.



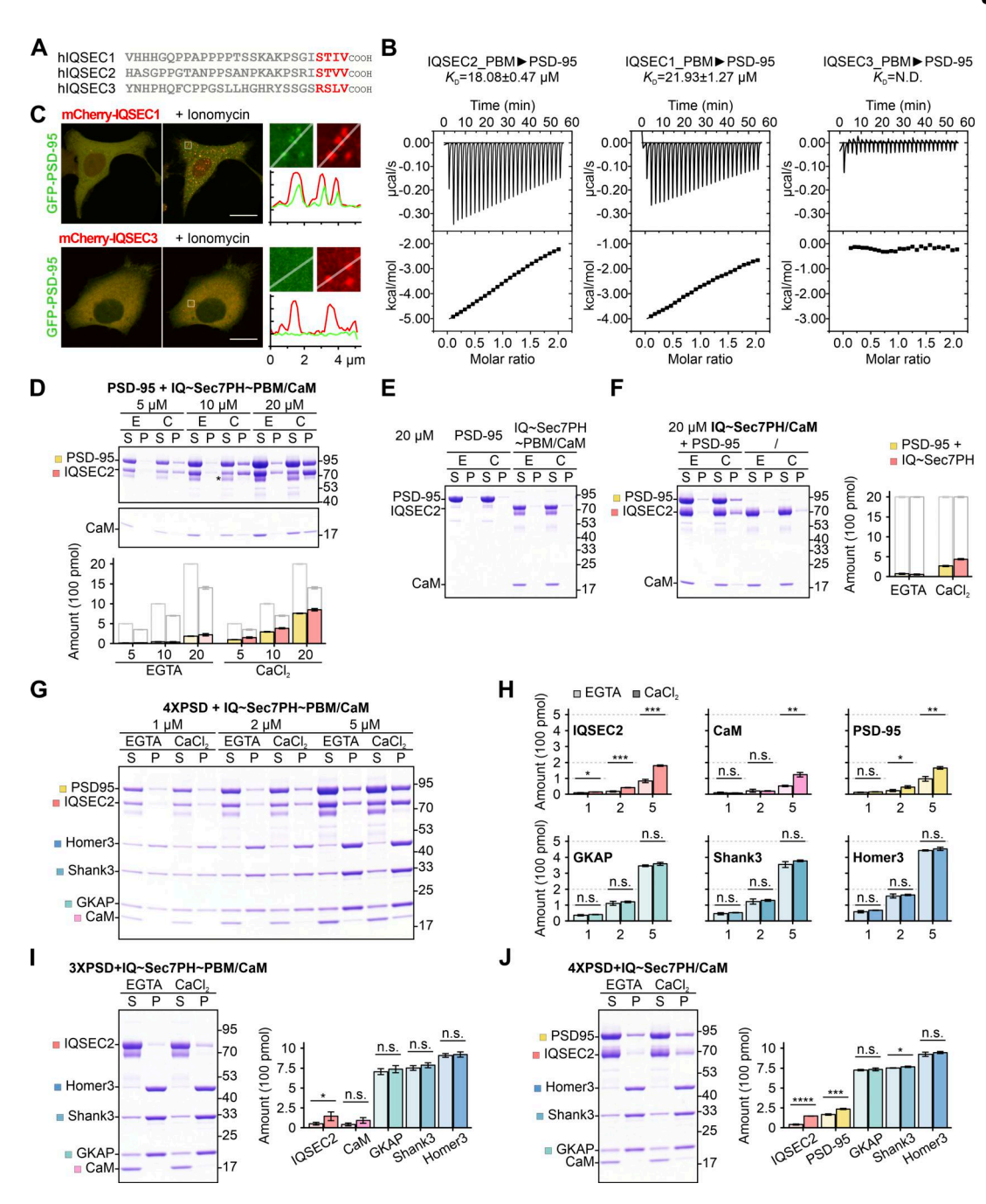


Figure S5. IQSEC2 phase separation promotes PSD-95 integration into the PSD condensates. (A) The C-terminal aa sequence of IQSECs. The PBM is highlighted. (B) The ITC curve of 200 µM IQSECs_PBM titrating into 20 µM PSD-95 protein. N.D., not detectable. (C) Overexpressed GFP-PSD-95 cocondensated with mCherry-IQSEC1, but not with mCherry-IQSEC3, in HeLa cells upon ionomycin stimulation. Fluorescence intensity line-scanning plots show that PSD-95 and IQSEC1 were concentrated and colocalized together in the bright puncta shown in the zoomed-in images. Scale bar, 20 µm. (D) Representative SDS-PAGE of sedimentation experiments (upper panel) and quantification of protein distributions in the supernatant and pellet (lower panel) showing that the involvement of PSD-95 lowered the threshold concentration of Ca²⁺-induced phase separation of IOSEC2. Note that degraded proteins (*), which lost the C-terminal PBM, did not co-condensate with PSD-95 and were excluded during quantification. Data from three repeated experiments were presented as mean ± SD. (E) Control experiments showing that PSD-95 and IQ~Sec7PH~PBM/CaM alone do not form condensates at 20 μM in solution. (F) Control experiments showing that the PBM region is required for IQSEC2 to bind to PSD-95 and to undergo co-sedimentation. The input concentration of each component was 20 μM. Data from three repeated experiments were presented as mean ± SD. (G and H) Representative SDS-PAGE of sedimentation experiments and quantification of protein amounts in the pellet showing that Ca²⁺-induced IQSEC2 phase separation promotes PSD-95 integration into the PSD assembly. Data from three repeated experiments were presented as mean ± SD (n.s., not significant; *P < 0.05; **P < 0.01; ***P < 0.001; ****P < 0.0001; unpaired t test). (1) Control experiments showing that PSD-95 is required for IQSEC2 co-sedimented with the PSD assembly. The input concentration of each component was 10 μ M. Data from three repeated experiments were presented as mean \pm SD (n.s., not significant; *P < 0.05; unpaired t test). (1) Control experiments showing that the PBM is required for IQSEC2 co-sedimented with the PSD assembly. The input concentration of each component was 10 µM. Data from three repeated experiments were presented as mean ± SD (n.s., not significant; *P < 0.05; ***P < 0.001; ****P < 0.0001; unpaired t test). Source data are available for this figure: SourceData FS5.

Bai et al. Journal of Cell Biology



Video 1. Related to Fig. 4 A, showing the puncta fusion process in response to calcium influx in HeLa cells expressing mCherry-IQSEC2. Scale bar, 20 μm.